

To appear in *The Astrophysical Journal*.

## The Asymmetric Wind in M82

P. L. Shopbell<sup>1</sup>

Rice University, Department of Space Physics & Astronomy, MS 108, Houston, TX 77251;  
pls@astro.caltech.edu

and

J. Bland-Hawthorn

Anglo-Australian Observatory, P.O. Box 296, Epping, NSW 2121, AUSTRALIA;  
jbh@aaoepp2.aao.gov.au

### ABSTRACT

We have obtained detailed imaging Fabry-Perot observations of the nearby galaxy M82 in order to understand the physical association between the high-velocity outflow and the starburst nucleus. The high spatial and kinematic resolution of our observations has allowed us to perform photometric analyses of H $\alpha$ , [N II], and [O III] spectral lines at roughly one hundred thousand positions across the extent of the galaxy.

The observed velocities of the emitting gas in M82 reveal a bipolar outflow of material, originating from the bright starburst regions in the galaxy's inner disk, but *misaligned* with respect to the galaxy spin axis. The deprojected outflow velocity indicated by the optical filaments increases with radius from 525 to 655 km s<sup>-1</sup>. All three spectral lines show double components in the centers of the outflowing lobes, with the H $\alpha$  line split by  $\sim 300$  km s<sup>-1</sup> over a region almost a kiloparsec in size. The filamentary lobes lie along an axis tilted by 15° with respect to the spin axis, confirmed by the regions of line splitting and the ionization pattern over the outflow. The filaments are not simple surfaces of revolution, nor is the emission distributed evenly over the surfaces. We model these lobes as a composite of cylindrical and conical structures, collimated in the inner  $\sim 500$  pc but expanding at a larger opening angle of  $\sim 25^\circ$  beyond that radius. We compare our kinematic model with simulations of starburst-driven winds in which disk material surrounding the source is entrained by the wind. There is some evidence for rotation of the wind filaments about the outflow axis in support of entrainment, and we find strong similarities between the observed and predicted structures.

---

<sup>1</sup>Current address: California Institute of Technology, 105-24, Pasadena, CA 91125

The data reveal a remarkably low  $[\text{N II}]/\text{H}\alpha$  ratio in the region of the outflow, indicating that photoionization by the nuclear starburst may play a significant role in the excitation of the optical filament gas, particularly near the nucleus. An increase in the  $[\text{O III}]/\text{H}\alpha$  ratio along the outflow is observed. At larger radii, the line diagnostics and a strong spatial correlation between  $\text{H}\alpha$  and soft x-ray filaments are consistent with shock ionization.

A smooth spherical halo around M82 is observed in emission lines, extending to at least 2 kpc. We propose that the dusty halo is the primary source of the linearly polarized optical emission. A diffuse ionized medium (DIM) with enhanced  $[\text{N II}]/\text{H}\alpha$  emission pervades throughout the stellar disk. We discuss likely sources of ionization and heating.

*Subject headings:* galaxies: individual (M82, NGC 3034); galaxies: starburst; ISM: jets and outflows; galaxies: kinematics and dynamics; techniques: interferometric

## 1. Introduction

Ten years ago Chevalier and Clegg (1985) published a brief letter in which they conjectured that a high supernova rate in a galactic nucleus could heat the surrounding gas to temperatures with sound speeds exceeding the escape velocity of the galaxy. This hot, tenuous gas would expand outward from the galaxy in the form of a “wind,” enriching the surrounding intergalactic medium. Since that time, the galactic wind model has been confirmed by observations of over a dozen galactic-scale outflows: e.g., M82 (Axon & Taylor 1978), NGC 253 (Fabbiano & Trinchieri 1984), NGC 1569 (Heckman *et al.* 1995), NGC 1705 (Meurer, Freeman, & Dopita 1989), NGC 1808 (Phillips 1993), NGC 2146 (Armus *et al.* 1995), NGC 3079 (Veilleux *et al.* 1994), NGC 3628 (Fabbiano, Heckman, & Keel 1990), NGC 4051 (Christopoulou *et al.* 1997), NGC 4666 (Dahlem *et al.* 1997), M82 (Phillips *et al.* 1983). These massive ejections of gas and dust are usually observed as large ( $\sim$ few kpc), roughly conical structures of filaments originating in the nuclear regions and oriented along the minor axes of the galaxies. They are therefore most often observed in edge-on disk systems (e.g., M82, NGC 1808), in optical emission lines (Lehnert & Heckman 1995), radio continuum (Baum *et al.* 1993), and soft X-rays (e.g., Bregman, Schulman, & Tomisaka 1995; Armus *et al.* 1995). Recent spectral studies have also shown the ability to detect winds in face-on galaxies using their kinematic signatures (e.g., NGC 2782 [Boer, Schulz, & Keel 1992], M82 [Hamilton & Keel 1987; Krabbe *et al.* 1997]).

In some cases these winds are indeed driven by supernovae and massive stellar winds from a central starburst (e.g., M82, NGC 1569; Lehnert & Heckman 1995; Lehnert & Heckman 1996), while other winds appear to be powered by more exotic forces associated with the central engines of AGN (e.g., NGC 3079, NGC 4051; Colbert *et al.* 1996a; Colbert *et al.* 1996b), and some galaxies appear to exhibit both starburst and AGN characteristics (e.g., NGC 1808 [Forbes, Boisson, &

Ward 1992], M82 [Lípari, Colina, & Macchetto 1994]). Because of the low densities of the wind material, emission from optical lines is often very difficult to detect, except in nearby galaxies. The x-ray emission from these winds is comparable in luminosity to the optical emission lines, but is visible on larger spatial scales and therefore detectable to greater distances.

Due to its proximity and favorable inclination angle (see Tab. 1), the irregular disk galaxy M82 (NGC 3034) has been studied extensively as a prototype galactic wind system. Following the original discovery (Lynds & Sandage 1963), the first detailed spectroscopic study of the optical emission line filaments (Burbidge, Burbidge, & Rubin 1964) revealed kinematics indicative of a bipolar, roughly conical, outflow of gas along the minor axis of the galaxy.

Thirty years and over 500 published papers later, the initial interpretation of the M82 filaments in terms of an outflow still stands. Support for this picture extends from radio to gamma ray wavelengths. The starburst nature of the nucleus of M82 has been verified through its strong infrared emission (e.g., Soifer, Houck, & Neugebauer 1987; Rice *et al.* 1988; Telesco *et al.* 1991) and numerous compact radio supernovae (e.g., Kronberg, Biermann, & Schwab 1985; Huang *et al.* 1994; Muxlow *et al.* 1994). Models of the starburst evolution produce appropriate quantities of energy and mass on plausible timescales to create and sustain the observed nuclear and galactic wind behavior (e.g., Rieke *et al.* 1993; Doane & Mathews 1993). The wind itself has been observed optically in both spectral (e.g., McCarthy, Heckman, & van Breugel 1987; McKeith *et al.* 1995) and imaging studies (e.g., Ichikawa *et al.* 1994), in emission lines (e.g., Armus, Heckman, & Miley 1990) and broadband radiation (e.g., O’Connell & Mangano 1978). In particular, kinematic evidence for the existence of a galactic wind in M82 has been presented by several optical emission line studies (e.g., Heckathorn 1972; Axon & Taylor 1978; Bland & Tully 1988; Heckman, Armus, & Miley 1990; McKeith *et al.* 1995), and even by molecular observations (Nakai *et al.* 1987).

An extensive x-ray halo has been observed oriented along the minor axis, extending 5–6 kpc from the disk, far beyond the visible extent of the optical filaments (e.g., Watson, Stanger, & Griffiths 1984; Schaaf *et al.* 1989; Bregman, Schulman, & Tomisaka 1995). A few percent of the supernova energy from the starburst has been deposited in this hot ( $T \sim 10^8$  K) “x-ray wind.” A large ( $r \sim 8$  kpc) spherical halo has been reported at radio continuum wavelengths (Seaquist & Odegard 1991), and has been interpreted as synchrotron emission from relativistic electrons in the outflowing wind.

With this wealth of data, it is surprising that little attempt has been made to undertake detailed comparisons of models and observations. Large-scale galactic winds were first proposed to account for the lack of gas in elliptical galaxies (Mathews & Baker 1971). The theory of these winds has since evolved in tandem with research on starburst-driven galactic winds (e.g., White & Chevalier 1983; Smith, Kennel, & Coroniti 1993a; Smith, Kennel, & Coroniti 1993b). Since the original starburst wind model (Chevalier & Clegg 1985), advances have been made in both analytical studies (e.g., Koo & McKee 1992a; Koo & McKee 1992b) and hydrodynamic simulations (e.g., Tomisaka & Ikeuchi 1988; Tomisaka & Bregman 1993; Suchkov *et al.* 1994;

Suchkov *et al.* 1996). Models of winds in other astrophysical situations, such as stellar winds (e.g., Shu *et al.* 1991) and winds from AGN (e.g., Smith 1993; Arav & Li 1994; Arav, Li, & Begelman 1994), have contributed to our understanding as well. On a broader scale, starburst-driven winds have important ramifications for a variety of astrophysical and cosmological situations, including enrichment of the intergalactic medium, contributions to the diffuse X-ray background, the evolution of dwarf and interacting galaxies, and the formation of elliptical galaxies through mergers (see Heckman, Armus, & Miley 1990 and references therein).

Toward the goal of investigating this model, we have obtained high-resolution imaging Fabry-Perot observations of M82 in several optical emission lines. In Section 2 of this paper we present our Fabry-Perot observations and describe the methods of data reduction. In Section 3, we present the derived two-dimensional emission-line maps of M82 illustrating the distribution of line flux, ionized gas velocity, and ionization state across the outflow. In Section 4, we describe our new data for the disk, halo, and outflow and provide comparisons with other published observations and a number of kinematic models. We present our conclusions in Section 5. A subsequent paper describes refinements to our kinematic and ionization models to accommodate new observations from the *Keck* and *Hubble Space Telescopes*.

## 2. Observations and Reductions

### 2.1. Fabry-Perot Observations

Observations of M82 were obtained in February, 1986 at the 3.6-meter Canada-France-Hawaii telescope (CFHT) on Mauna Kea, in the emission lines of  $H\alpha$   $\lambda 6563$  and  $[N\ II]\ \lambda 6583$ . The Hawaii Imaging Fabry-Perot Interferometer (HIFI; Bland & Tully 1989) was used with an ET-50 etalon from Queensgate Instruments. The etalon coatings were formulated to provide a free spectral range of  $85\text{\AA}$  and a finesse of 60, for a spectral resolution of  $1.4\text{\AA}$  ( $65\text{ km s}^{-1}$ , at  $H\alpha$ ). The  $512 \times 512$  pixels of the Texas Instruments CCD, after  $2 \times 2$  on-chip binning, each subtend  $0''.86$  ( $\sim 13\text{ pc}$  at the distance of M82). This scale undersampled the estimated  $1''$  seeing disk but was necessary due to the low flux levels of the outflow emission. The  $3'.5$  field covers almost the entire region of minor-axis optical filaments. Other characteristics of the observing system are provided in Table 2, along with their experimentally determined values.

A second set of Fabry-Perot observations were obtained in March, 1992 at the University of Hawaii 88-inch telescope on Mauna Kea, in the emission line of  $[O\ III]\ \lambda 5007$ . Again the HIFI system was used, with an ET-70 etalon owned by Dr. Sylvain Veilleux. Although the free spectral range of this etalon ( $61\text{\AA}$ ) was smaller than that used for the  $H\alpha$  and  $[N\ II]$  observations, the finesse was essentially identical, as were the effective spatial and velocity resolutions ( $0''.85\text{ pix}^{-1}$  and  $60\text{ km s}^{-1}$  at  $[O\ III]$ , respectively) and the field of view. The characteristics of the observing system are provided in more detail in Table 2. In both cases, the etalon was tilted to remove internal reflections and paired with wide ( $50\text{\AA}$  FWHM) interference filters to eliminate interorder

confusion problems.

## 2.2. Data Reductions

Most of the data reduction was performed under the Zodiac image processing system (Miyashiro 1982; Shopbell 1997), encompassing standard routines as well as a number of programs written by the authors and optimized for Fabry-Perot data. IRAF<sup>2</sup> was also used for a small number of specific problems. A summary of the data reduction steps is now provided; see Shopbell 1995 for more details.

### 2.2.1. CCD Reductions

The bias level was subtracted from each frame, using the average of several CCD bias frames. Cosmic rays were denoted by hand and removed by nearest-neighbor interpolation. Bad columns were also denoted by hand and then removed by sinc interpolation across each row of the bad column. The sinc function was selected for use in the interpolation because of its favorable Fourier properties: its Fourier transform is the top-hat function, implying even sampling of the image noise structure over a finite range of frequency.

A flatfield image was constructed for our data by summing a series of frames of a white source, scanning the etalon through a free spectral range. Any first-order slope in the illumination pattern was removed with a two-dimensional linear fit. (Sky flats were not available.) The flatfield was then divided by a smoothed ( $\sigma \sim 3$  pixels) version of itself, normalized, and divided into each data and calibration frame. Due to problems with on-chip binning, the movement of transient defects between the images of each cube, and temperature fluctuations of the CCD, the flatfielding process did not substantially alter the noise content of most frames. Fortunately, the pixel-to-pixel sensitivity variations comprise a noise source at a level of only  $\sim 1.6\%$ , a small value compared to other Fabry-Perot photometry uncertainties.

### 2.2.2. Fabry-Perot Reductions

*Cube building.* In order to randomize variations in the sky background due to changing hour angle, approaching dawn, etc., as well as instrumental fluctuations, the data frames were observed in a random or staggered order with respect to the etalon optical gap. The frames were first sorted

---

<sup>2</sup>IRAF is distributed by the National Optical Astronomy Observatories, which is operated by the Association of Universities for Research in Astronomy, Inc. (AURA) under cooperative agreement with the National Science Foundation.

by gap and stacked to form cubes: target (M82) data cubes through each filter, a whitelight or flatfield cube through each filter, a standard lamp calibration cube, and standard star cubes.

*Whitelight calibration.* The whitelight cube was used to map the spatial and spectral shape of the interference filter, which was then removed in the same manner as flatfielding. The whitelight cube was heavily smoothed ( $\sigma \sim 15$  pixels) in the spatial dimension, re-sampled from  $0.65\text{\AA}$  to  $0.99\text{\AA}$  steps, to match the etalon gap spacings of the data cubes, then normalized and divided into the corresponding data cubes.

*Frame alignment.* The frames in each data cube were aligned using two stars near the disk of the galaxy. (The single bright star in the field, AGK 3+69 428 [Bettoni & Galletta 1982],  $2'.5$  southwest of the nucleus, saturated the detector.) Fractional pixel shifts were made by two-dimensional spline interpolation of the images. The spatial registration is accurate to better than one pixel ( $\lesssim 0''.5$ ).

We note here that, although the HIFI system and the tilted etalon provide a field that is relatively free of ghost reflections, the location of the bright star AGK 3+69 428 in the southwest corner of the frame was such that a pair of concentric ghost images of the star appear opposite the optical axis, in the southeast corner of the frame. Following frame registration, a region encompassing the ghost images was masked from further analysis. This is unfortunate, in that the minor axis emission of M82 runs directly through this region, but it demonstrates the care that must be taken when observing with Fabry-Perot systems, which always have prevalent ghost patterns.

*Ring fitting.* Temperature and humidity variations produce drifts in the the expected spectral response of the Fabry-Perot etalon. In order to parametrize the spectral and spatial drifts in the Fabry-Perot system, we obtained a set of calibration lamp images, taken periodically throughout the night, all at the same etalon spacing. Elliptical fits to the rings revealed no noticeable variations in the radius or circularity of the rings, indicating that the spectral stability of the etalon was extremely good. Flexure of the telescope system was detectable as a two pixel ( $\sim 1''.5$ ) shift of the ring centers (i.e., the optical axis) over the course of each night. The frame alignment procedure has removed this, with minimal effect along the wavelength axis.

*Data cube resampling and smoothing.* While our  $\text{H}\alpha$ + $[\text{N II}]$  data was sampled regularly at  $0.99\text{\AA}$  ( $45 \text{ km s}^{-1}$ ) intervals across the  $\text{H}\alpha$  line, observing time constraints required us to interpolate several frames across the  $[\text{N II}]$  portion of the spectra, where the sampling was a factor of two coarser. Although a spline interpolation was performed without difficulty, a slightly larger error should be assumed for the final  $[\text{N II}]$  fluxes and velocities. The  $[\text{O III}]$  data set required extrapolation of a single (continuum) frame at either end of the spectra.

A light Hanning filter was then applied along the spectral axis of each cube, in order to allow efficient automated fitting of the large numbers of the spectra. Tests indicate this had a negligible effect on the final fit parameters.

*Phase calibration.* The instrumental profile of a Fabry-Perot interferometer is a complex function of spatial position, wavelength, and optical gap spacing, given by the well-known Airy function (Bland & Tully 1989). Due to the large free spectral range and low interference order of the etalons, the monochromatic “phase surfaces,” as observed in the emission lines of a calibration lamp, were well parametrized by the analytical expression for the three-dimensional Airy function. A fit to this function determined several system constants listed in Table 2. This fit was then used to shift each spectrum in the data cube by the appropriate value to generate monochromatic frames. The convergence of two night sky lines into a single frame each confirmed the accuracy of the phase correction for the  $H\alpha + [N\ II]$  data set. For the  $[O\ III]$  data set, however, a poorly sampled calibration cube prevented us from performing an accurate phase correction. Therefore the  $[O\ III]$  observations will be used for flux measurements and morphology, but not for kinematic studies.

*Sky subtraction.* A limited field of view prevented us from obtaining a sky spectrum devoid of galaxy emission. We therefore removed the two bright night sky lines in the  $H\alpha + [N\ II]$  data set by subtracting Gaussian components with the proper velocity and a mean flux level as observed across the field. The lines were identified as OH emission at  $6553.61\text{\AA}$  and  $6577.28\text{\AA}$  (Osterbrock & Martel 1992), providing the wavelength calibration for the spectral axis. The night sky continuum was not removed from the data. The  $[O\ III]$  data were not sky-subtracted, due to the low level of sky flux and the difficulties associated with the non-phase-corrected data. Resulting errors in the final spectral fits are negligible.

### 2.2.3. Photometry

Recent studies (e.g., Veilleux *et al.* 1994) have shown that Fabry-Perot data can be flux calibrated to an accuracy equal to that of CCD imagery and longslit spectroscopy. Rather than scaling to an externally calibrated data set, we have applied a primary calibration, employing standard star observations directly. Since this Fabry-Perot flux calibration procedure is described in more detail elsewhere (e.g., Bland-Hawthorn *et al.* 1997), we outline only the salient points below.

The star  $\varepsilon$  Orionis was used to calibrate the  $H\alpha + [N\ II]$  observations;  $\alpha$  Lyrae and  $\eta$  Hydrae were used for the  $[O\ III]$  observations. After cosmetic cleaning and applying the whitelight correction described above, the counts in each stellar image were summed, and then scaled by the telescope aperture size and exposure time. To obtain pixel values in units of  $\text{counts cm}^{-2} \text{sec}^{-1} \text{\AA}^{-1}$  we must then divide by the effective spectral bandpass of the etalon at each pixel. We emphasize that this value is not necessarily the same as either the spectral sampling of the cube or the etalon resolution. Rather, it is a measure of the amount of flux transmitted at a given wavelength for a sequence of etalon spacings; it depends primarily on the finesse ( $N_R$ ) of the etalon. This “effective bandpass” was calculated by summing the flux under a synthetic monochromatic spectrum spanning an entire order of the appropriate theoretical Airy function

and dividing by the peak value of the Airy function. We derived an effective bandpass of  $3.0\text{\AA}$  for our data sets. The scaled values of observed stellar counts were then compared with published flux values (Hayes 1970; Hayes & Latham 1975), corrected for atmospheric extinction. Each pixel in the final spectra has units of  $\text{ergs cm}^{-2} \text{ sec}^{-1} \text{ pixel}^{-1} \text{ frame}^{-1}$ , yielding total fluxes from the line fits in units of  $\text{ergs cm}^{-2} \text{ sec}^{-1} \text{ pixel}^{-1}$ . The final estimated systematic error in the flux calibration was  $\sim 7.5\%$ .

### 3. Fabry-Perot Maps

The emission-line spectra were fit with Gaussian profiles across the field to generate spatial maps of line characteristics such as flux, velocity, and dispersion. Single-component fits were made to the  $\text{H}\alpha$  and  $[\text{N II}]$  lines across the majority of the field, well into the halo of the galaxy. There are regions north of the galaxy’s disk where double components were fit to the  $\text{H}\alpha$  line profile, as well as regions south of the disk where double components were fit to both the  $\text{H}\alpha$  and  $[\text{N II}]$  lines. The  $[\text{O III}]$  line was fit with a single Gaussian component throughout the field, although visual inspection revealed signs of line splitting in specific regions.

The region of acceptable fits is identical for the  $\text{H}\alpha$  and  $[\text{N II}]$  maps, although the  $[\text{N II}]$  fits in the northern-most regions of the maps have significantly higher errors, due to clipping of the  $6583\text{\AA}$  profile by the limited spectral coverage. The region with sufficient  $[\text{O III}]$  flux for profile fitting is much smaller than that of  $\text{H}\alpha$  or  $[\text{N II}]$ . The central regions of the galaxy are saturated in both the  $\text{H}\alpha$  and  $[\text{N II}]$  observations.

We now describe the important features of each Fabry-Perot map. Each spatial map is presented at approximately the same scale, with tick marks separated by one arcminute ( $\sim 950 \text{ pc}$ ). The maps from the  $\text{H}\alpha + [\text{N II}]$  data set contain regions in which the spectral lines are split; these maps show both a flux-weighted total for the galaxy as well as values for the individual components separately. These components are referred to as the high-velocity component (HVC) and the low-velocity component (LVC). North is up and east is to the left in all images. The position angle of the major axis of the galaxy is approximately  $65^\circ$ .

Figure 1 illustrates the flux distribution in the light of  $\text{H}\alpha$   $6563\text{\AA}$  and  $[\text{N II}]$   $6583\text{\AA}$ . We measure a total unsaturated  $\text{H}\alpha$  flux of  $9.9 \times 10^{-11} \text{ ergs cm}^{-2} \text{ sec}^{-1}$  and a total  $[\text{N II}]$  flux of  $4.1 \times 10^{-11} \text{ ergs cm}^{-2} \text{ sec}^{-1}$ . A rough comparison with the  $\text{H}\alpha$  imagery to be presented in the next section indicates that the saturated nuclear regions contribute an additional  $\sim 2.1 \times 10^{-11} \text{ ergs cm}^{-2} \text{ sec}^{-1}$  in the  $\text{H}\alpha$  line, or  $\sim 17\%$  of the total. The flux is concentrated in the nucleus and along the minor axis, with very little emission originating in the extended disk of the galaxy. The nuclear line emission has saturated the detector in two concentrations (“the eyes”), as well as a number of weaker ancillary regions. In contrast, the minor axis emission is spatially extensive and filamentary. Numerous long radial filaments can be seen extending more than a kiloparsec from the nucleus, as well as complex small-scale structures. Note, for example, the bright bow



shock-like arc approximately 500 pc SSE of the nucleus.

The morphology of the extraplanar gas differs between the two sides of the galaxy, appearing more chaotic on the north side and showing signs of collimation in the south. The southern  $H\alpha$  emission exhibits a sharp edge on the eastern side. Furthermore, the emission to the south is considerably brighter and more extensive, although there appears to be an abrupt reduction in flux at a distance of approximately 500 pc from the nucleus. Examination of the  $H\alpha$  and  $[N II]$  emission maps reveals that, beyond 500 pc, the flux in the HVC drops rapidly, while the flux in the LVC remains more uniform. We also find pervasive diffuse emission at a low level throughout the halo of the galaxy.

Figure 2 is a map of the flux from M82 at  $[O III] 5007\text{\AA}$ . We measure a total  $[O III]$  flux of  $2.6 \times 10^{-12} \text{ ergs cm}^{-2} \text{ sec}^{-1}$ , more than an order of magnitude below that seen at  $H\alpha$  and  $[N II]$ . There is essentially no emission from the disk at this wavelength; the flux originates almost entirely within the nucleus and along the southern minor axis of the disk. Although the radial extent of the minor-axis emission is much smaller than that seen in  $[N II]$  and  $H\alpha$ , the filamentary morphology is similar. Indeed, excellent correlation is seen with the  $H\alpha$  flux map, which has been contoured on Figure 2. A striking feature of the  $[O III]$  flux map is the presence of two distinct streams of emitting gas, each extending along the southern minor axis from one of the bright nuclear emission regions. These streams can also be identified in the  $H\alpha$  flux map (Figure 1), although the much more pervasive nature of the  $H\alpha$  emission makes the structure more difficult to discern at small radii.

Figure 3 is a radial velocity map for the  $H\alpha$ -emitting gas in M82. Two prominent trends are seen: first, there exists a strong velocity gradient along the major axis of the galaxy, consistent with normal disk rotation, with the eastern end moving away from the observer. Second, a velocity transition is evident along the minor axis of the galaxy: strong blue-shifting of the  $H\alpha$  emission is seen south of the disk; strong red-shifting to the north. The major-axis rotation signature merges into this minor axis motion in a gradual fashion, although this may be due in part to the flux-weighting procedure.

The HVC consists of highly redshifted emission in the north and highly blueshifted emission in the south ( $v_r \sim 300 \text{ km s}^{-1}$ ). The LVC consists of emission at roughly the systemic velocity of the galaxy ( $v_{sys} \approx 203 \text{ km s}^{-1}$ ; de Vaucouleurs *et al.* 1991), in both the north and south. The northern and southern component pairs mirror each other almost exactly in terms of relative velocity and kinematic structure. Perhaps surprisingly, the velocities within each individual component exhibit little radial or azimuthal variation. The exception to this is the inner portion of the HVC, where the radial velocities approach the systemic velocity.

A map of the line-of-sight velocities of the  $[N II]$ -emitting gas was also produced, but is not presented here, as it provides little additional information. The trends along both the major and minor axes are identical to those seen at  $H\alpha$ , but at a lower signal-to-noise ratio due to the decreased flux of  $[N II]$  line emission. A velocity map of the  $[O III]$ -emitting gas was not produced,

for the reasons outlined above.

Figure 4 shows the logarithm of the ratio of the [N II] 6583Å flux to the H $\alpha$  6563Å flux from M82. The most remarkable feature in this map is the presence of a distinct region of low line ratio (0.0–1.0) along the minor axis, south of the disk. This region extends at least a kiloparsec in radius from the nucleus and is narrower than the regions of minor axis filaments visible in the H $\alpha$  and [N II] flux maps (Fig. 1). The region of low ratios can be separated into two distinct structures, originating with the bright central eyes of M82, similar to the structures seen at smaller radii in the [O III] 5007Å flux map (Fig. 2).

Elsewhere in the galaxy, higher line ratios ( $\gtrsim 1.0$ ) prevail, particularly at large radii within the inclined disk. Discrete H II regions can be seen in the disk as small concentrations with the expected [N II]/H $\alpha$  ratio of  $\sim 0.5$  (Osterbrock 1989). The regions of extremely low line ratio to the north are a result of the incompletely sampled [N II] line, and should be ignored.

Figure 5 is a map of the logarithm of the ratio of the [O III] 5007Å flux to the H $\alpha$  6563Å flux from M82. The ratio has been calculated over the entire spatial extent of the [O III] emission, as seen in the flux map (Fig. 2). The observed ratios are low ( $\sim 0.05$ ) throughout the nucleus and regions south of the disk, with the only apparent trend being a gradual increase in the ratio with distance from the nucleus.

## 4. Discussion

We now discuss the observational implications of these data in the context of each of the galaxy’s primary morphological components: starburst disk, extended halo, and galactic-scale outflow.

### 4.1. Starburst Disk

Our observations reveal a small irregular disk containing heavy obscuration and a central starburst. The H $\alpha$  and [O III] flux maps (Figs. 1 and 2) reveal little ionized gas in the extended disk of M82, outside of the central nuclear starburst region, as found by slit spectra (O’Connell & Mangano 1978). Small concentrations of line emission that do exist in the disk outside of the starburst, such as the regions 0’.5 east of the nucleus (see also O’Connell & Mangano 1978; Fig. 3), appear to be giant H II regions. The [N II]/H $\alpha$  ratio map (Fig. 4) indicates moderate values for these regions ( $\sim 0.56$ ), consistent with a cooler range of photoionized H II regions ( $T_{\text{max}} \sim 40,000$  K, Evans & Dopita 1985; Veilleux & Osterbrock 1987). Such regions exhibit low levels of [O III] emission, consistent with our non-detection in Figure 2. Although the high extinction in the disk of M82 (3–27 mag; O’Connell *et al.* 1995; McLeod *et al.* 1993) serves to hide smaller H II regions from our optical observations, the paucity of large H II regions suggests that

the level of star formation must be low outside of the central starburst. This conclusion has also been reached by multi-epoch radio supernovae studies (e.g., Kronberg, Biermann, & Schwab 1985; Huang *et al.* 1994). The weak nature of the [O III] emission implies a high overall metallicity in M82, as has been suggested by previous observations (e.g., Duffy *et al.* 1987; Gaffney & Lester 1992), and as is anticipated due to chemical enrichment by the starburst (e.g., Kobulnicky & Skillman 1996).

The nuclear emission is dominated by two large saturated regions, each approximately 200 pc in diameter, and centered  $\sim 125$  pc from the  $2\ \mu\text{m}$  stellar nucleus (see Fig. 1). These regions correspond to knots *A* and *C* of O’Connell & Mangano 1978 and are known to be extremely high surface brightness “clusters of clusters” of young ( $T \lesssim 50$  Myr) stars (O’Connell *et al.* 1995). Also identifiable in Figure 1 are knots *D* and *E* (also saturated), as well as knots *F*, *G*, and *H*. Knot *B* is extremely faint at  $\text{H}\alpha$  wavelengths, especially when compared to broadband (O’Connell & Mangano 1978) and ultraviolet (Hennessy 1996) observations, suggesting a higher gas content in the inner regions of the galaxy. The outflow can be traced to knots *A* and *C*. This relationship is particularly well-demonstrated by the [N II]/ $\text{H}\alpha$  map (Fig. 4) and the [O III] flux map (Fig. 2).

We have plotted the  $\text{H}\alpha$  radial velocities along a straight line corresponding to the major axis of the galaxy in Figure 6 (panel *c*), along with a number of rotation curves from the literature at a range of wavelengths. The published systemic velocity of M82,  $203\ \text{km s}^{-1}$  (de Vaucouleurs *et al.* 1991), corrected to a heliocentric value of  $208.7\ \text{km s}^{-1}$ , has been subtracted from the  $\text{H}\alpha$  Fabry-Perot data. The rotation curve rises to approximately  $100\ \text{km s}^{-1}$  within  $\sim 9''$  ( $\sim 140$  pc) of the nucleus and remains relatively flat to the edges of the observations. No substantial fall-off in the rotation curve is seen, due primarily to the limited radial extent of line emission from the disk. The observed rotation curve matches well those found at  $\text{H}\alpha$  by Heckathorn 1972 (his Fig. 12) and McKeith *et al.* 1993 (panel *d* of Fig. 6), including the turn-over and asymptotic velocities and the nuclear velocity gradient ( $\sim 11\ \text{km s}^{-1}\ \text{arcsec}^{-1}$ ). Figure 6 also illustrates an increase in the central velocity gradient with wavelength. As has been pointed out by other authors (e.g., McKeith *et al.* 1993), this effect is indicative of the large extinction toward the nuclear regions of the galaxy.

The  $\text{H}\alpha$  rotation curve also correlates well with that of the 250 pc nuclear ring seen in molecular emission lines (e.g., Loiseau *et al.* 1990). The double-lobed structure of the central  $\text{H}\alpha$  emission is suggestive of an edge-on ring structure as well, interior to the molecular ring. The starburst could be identified with the ring of ionized gas and is probably propagating outward, fueled by the cold gas in the molecular ring (Waller, Gurwell, & Tamura 1992; cf. Shen & Lo 1995). This ring may also provide much of the extinction toward the nucleus of M82 (e.g., Telesco & Gezari 1992). The dynamic conditions of the central regions would have removed most of the obscuring material interior to the ring, as has been suggested in our Galaxy (e.g., Becklin, Gatley, & Werner 1982). The resolution of the central star clusters by recent HST observations (O’Connell *et al.* 1995) suggests that any such ring would be very clumpy however, and the two bright regions may indeed represent real spatial enhancements in the distribution of ionized gas and star formation. The relationship between this ring structure and the proposed bar in M82

( $r \sim 500$  pc; Telesco *et al.* 1991; Achtermann & Lacy 1995) is not clear.

The  $[\text{N II}]/\text{H}\alpha$  line ratio map (Fig. 4) shows a high ratio in the disk, especially at large radii, where the value is observed to exceed 1.0. The actual line ratios in the disk may be even slightly higher and possibly more uniform, due to dilution by the central starburst and the halo. Such high ratios are by no means rare in the nuclei of disk galaxies (Keel 1983), particularly LINERS (e.g., NGC 4319 [Sulentic & Arp 1987], NGC 5194 [Ford *et al.* 1985; Goad & Gallagher 1985]), and are understood to originate with shock excitation and/or photoionization by a power-law source (Veilleux & Osterbrock 1987). Although it is unlikely that M82 harbors an AGN (e.g., Rieke *et al.* 1980; Colina & Pérez-Olea 1992; Muxlow *et al.* 1994), a comparison with other galaxies which exhibit pervasive high  $[\text{N II}]/\text{H}\alpha$  line ratios in their extended disks is instructive: studies of NGC 3079 (Veilleux *et al.* 1994) and especially NGC 1068 (Bland-Hawthorn, Sokolowski, & Cecil 1991) have found high  $[\text{N II}]/\text{H}\alpha$  ratios of 0.6–1.3 across much of the inner disk. In NGC 1068, the disk H II regions are found to reside in regions of lower  $[\text{N II}]/\text{H}\alpha$  ratio ( $\sim 0.3$ – $0.8$ ), while the disk as a whole is permeated with gas exhibiting the higher ratios, similar to what we observe in M82. In order to boost this forbidden line to recombination line ratio, the “heating per ionization” must be high, for which most models require high energy photons, energetic electrons, or a dilute radiation bath (Sokolowski 1992).

In the case of M82, an attractive candidate to enhance the  $[\text{N II}]/\text{H}\alpha$  ratio in the disk is the concept of “mixing layers” (Slavin & Cox 1993; Voit, Donahue, & Slavin 1994). The turbulence resulting from the interaction of hot supernovae remnants with the ambient ISM creates an intermediate temperature phase, which models suggest emits a radiation field somewhat harder than thermal bremsstrahlung. This process can produce  $[\text{N II}]/\text{H}\alpha$  ratios in excess of 1.0 (Slavin, Shull, & Begelman 1993). By employing soft X-rays as the photoionization mechanism, mixing ratios have been used to model line emission ratios of up to 3–4 in cooling flows (Donahue & Voit 1991; Crawford & Fabian 1992). Considering the current optical appearance of the disk of M82, its interaction with the galaxy M81 approximately  $10^8$  years ago, and the energetic activity associated with the nuclear starburst, a turbulent inner disk would not be unexpected.

However, as mentioned above, our observations do not detect significant numbers of star forming regions outside the starburst nucleus. Even if this is attributed to high levels of extinction in the disk, other wavebands confirm the low level of star formation. All of the radio supernovae discovered by Kronberg, Biermann, & Schwab 1985 are within 300 pc of the galaxy’s nucleus, well inside the region of highest  $[\text{N II}]/\text{H}\alpha$  ratios. The diffuse X-ray flux in the disk has also been shown to decrease rapidly with radius, implying a reduced star formation rate outside the nuclear regions (Bregman, Schulman, & Tomisaka 1995). Other models for producing high  $[\text{N II}]/\text{H}\alpha$  ratios in the disk must be considered, such as chemical enrichment and cosmic ray heating. A combination of shock and photoionization may also provide a solution (e.g., Hunter & Gallagher 1990), although detailed models are not yet available.

## 4.2. Extended Halo

Early polarization observations detected a strong linear polarization throughout the halo of M82, with the position angles oriented perpendicular to a radial vector from the nucleus (Elvius 1969). This polarization was interpreted as evidence for a scattering component in the galaxy (e.g., Solinger 1969), probably consisting of electrons illuminated by the nucleus. The more difficult issue has been the polarization of the optical filaments themselves. The first observations in this regard (Visvanathan & Sandage 1972) determined that the minor axis filaments and the halo were equally polarized at optical wavelengths, suggesting that perhaps there was no “explosion” in M82 and that the off-axis filaments were merely density enhancements in a dusty cloud through which the galaxy was moving (Solinger, Morrison, & Markert 1977).

Although the discovery of split emission lines (Axon & Taylor 1978) and the minor-axis X-ray halo (Watson, Stanger, & Griffiths 1984) have virtually eliminated this alternate interpretation for the optical filaments (although see Rohan, Morrison, & Sadun 1987), the polarization measurements remain poorly understood. Recent observations (e.g., Scarrott, Eaton, & Axon 1991) indicate that the optical filaments may indeed contain a scattered component, but even then there is uncertainty as to the source of the polarization, i.e. the nucleus (Visvanathan 1974) or the entire disk (Solinger & Markert 1975). Unfortunately, with few exceptions (e.g., Schmidt, Angel, & Cromwell 1976; Bland & Tully 1988; Doane 1993; Suchkov *et al.* 1994), the presence of a halo component in M82 has been largely ignored.

Our detailed analyses in H $\alpha$  and [N II] clearly confirm the existence of the smooth exponential halo noted by Bland & Tully 1988. Figure 7 illustrates the flux along a narrow ( $\sim 9''$ ) band parallel to and approximately  $45''$  southeast of the major axis of the galaxy. The flux due to the outflow filaments can be seen superimposed upon an exponentially decreasing background. The halo has been detected across our entire region of fit lines, approaching a flux level of  $10^{-15}$  ergs cm $^{-2}$  sec $^{-1}$  arcsec $^{-2}$  at a radius of 1 kpc.

We have estimated the radial profile of the halo flux at H $\alpha$  with an exponential function:

$$I(\text{H}\alpha) = I_0(\text{H}\alpha)e^{-r/r_e}, \quad (1)$$

where  $I_0(\text{H}\alpha) \sim 1.6 \times 10^{-15}$  ergs cm $^{-2}$  sec $^{-1}$  arcsec $^{-2}$  Å $^{-1}$  and  $r_e \sim 315$  pc. This profile has been overlayed on the cut in Figure 7. For the observed halo line width of  $\sim 350$  km s $^{-1}$ , the integrated H $\alpha$  flux is  $\sim 2.5 \times 10^{-11}$  ergs cm $^{-2}$  sec $^{-1}$ . This compares with an observed flux from the filaments and *unsaturated* nucleus of  $\sim 9.9 \times 10^{-11}$  ergs cm $^{-2}$  sec $^{-1}$ . For a distance of 3.25 Mpc this implies a total H $\alpha$  luminosity from the halo of  $3.2 \times 10^{40}$  ergs sec $^{-1}$ .

The azimuthally symmetric polarization pattern of the halo in broadband light (Schmidt, Angel, & Cromwell 1976) suggests a scattering origin. The halo is known to comprise cold neutral atoms (Cottrell 1977), relativistic electrons (Seaquist & Odegard 1991), dust (Visvanathan & Sandage 1972) and warm ions (Bland & Tully 1988). If we associate the line-emitting halo with the polarized component, the line width ( $\sim 350$  km s $^{-1}$  FWHM) reflects either the motion of

scattering mirrors embedded in a warm medium or the “beam-averaged” projected kinematics of the nuclear and large-scale disk gas. If the observed line dispersion arises from thermal motions of electrons, the kinetic temperature must be less than 1000 K, at which point the flux from recombination would overwhelm the scattered flux for any reasonable halo density ( $n_H \approx 1 \text{ cm}^{-3}$ ; Cottrell 1977). Dust scattering is expected to be much more efficient in any case. The ratio of the scattering optical depths can be written

$$R_{de} = \frac{\sigma_d n_d}{\sigma_e n_e}, \quad (2)$$

where  $n_d$  and  $n_e$  are the dust and electron densities;  $\sigma_d$  and  $\sigma_e$  are the dust and electron scattering cross sections. For  $\sigma_d$ , we form the more conservative weighted mean of the MRN (Mathis, Rumpl, & Nordsieck 1977) grain distribution for which  $\sigma_d \approx 0.01 \mu\text{m}$ . In the local ISM, the dust-to-gas *number* density ratio is  $n_d/n_H \approx 10^{-12}$  (Ostriker & Silk 1973) although this depends strictly on the grain composition. With the conservative assumption of a totally ionized halo, we deduce a scattering ratio  $R_{de} \sim 50$ , verifying the relative importance of dust scattering. Schmidt, Angel, & Cromwell 1976 demonstrate that a reasonable optical depth to dust scattering is  $\tau_d \sim 0.1$  from a comparison of the halo broadband flux and the estimated disk flux.

The halo dust could reside in an extended neutral or warm ionized medium, some fraction of which could be supplied by the energetic wind (Burbidge, Burbidge, & Rubin 1964). We now compare the timescale for dust destruction by sputtering with the estimated age of the starburst wind,  $\tau_{wind} \sim 3 \times 10^6$  years (e.g., Lynds & Sandage 1963; Bland & Tully 1988). From Ostriker & Silk 1973, the timescale for grain sputtering is

$$\tau_{sput} \sim 3 \times 10^5 n_e \left( \frac{10^6}{T_e} \right)^{1/2} \left( \frac{0.01}{Y} \right) \left( \frac{r_d}{0.1} \right) \text{ years}, \quad (3)$$

where  $Y$  is the sputtering “yield,” i.e., the number of atoms released per impact.  $Y$  varies from  $\sim 5 \times 10^{-4}$  at the threshold sputtering temperature of  $3 \times 10^5$  K to  $\sim 0.01$  for temperatures of  $10^7$ – $10^8$  K.

At the low temperatures expected in a galactic halo,  $T \lesssim 10^5$  K, the lifetime of dust is greater than  $10^7$  yrs, comparable to or longer than the lifetime of the outflow. However, any dust located directly in the hot ( $T \sim 10^8$  K) X-ray-emitting wind survives for no more than  $10^5$  years, and has therefore been destroyed. Such an effect is supported by low-resolution radio maps of the M81/M82 region, which indicate an anti-correlation between the wind lobes and H I column density (Cottrell 1977). We note that more recent studies of gas-grain sputtering and grain-grain collisions (Tielens *et al.* 1994; Jones, Tielens, & Hollenbach 1996) suggest that grains may be able to survive much longer than previously thought. However, most of these studies are specific to the three-phase ISM in the Galaxy, and it remains unclear precisely how the results should be extended to galactic wind systems, which characteristically involve higher temperatures ( $10^8$  K vs.  $10^6$  K) and larger velocities ( $600 \text{ km s}^{-1}$  vs.  $200 \text{ km s}^{-1}$ ) than standard ISM models.

Given the sputtering timescales, if the dust has been delivered into the halo by the wind, it must be as a component of cooler material entrained by the hot wind itself. However, this implies that the halo dust and optical emission line filaments may then have the same origin and morphology, yet the polarization observations do not seem to indicate a minor-axis concentration in the dust distribution (Solinger & Markert 1975; Schmidt, Angel, & Cromwell 1976; Scarrott, Eaton, & Axon 1991). We also do not observe substantial redshifted emission south of the galaxy, as would be expected from mirrors moving with the outflow.

Alternatively, dust may have been forced into the halo at an early stage of the outflow, at a time when it was dominated much more by radiation from massive stars in the central burst than by supernovae. Such a mechanism has been hypothesized by Ferrara 1997 to explain the appearance of high- $z$  dust in the Galaxy and other edge-on spirals. It has been demonstrated that radiation pressure is sufficient to evacuate a large fraction of the dust near an active star-forming region into the halo, creating a dust distribution which varies slowly with height above the disk. Given the current importance of radiation effects in the inner portion of the M82 outflow (see Section 4.3.6 below) and the extensive nature of the observed dusty halo, such a scenario seems a reasonable model.

Regardless of any mechanism of relocating disk dust into the halo, clearly the hypothesized encounter between M81 and M82  $\sim 10^8$  years ago (Cottrell 1977; Yun, Ho, & Lo 1994) has played an important role in the evolution of the halo in M82. (This encounter is also thought to have initiated the central starburst in M82, e.g., Mihos & Hernquist 1994.) Radio observations have shown massive clouds of H I surrounding both galaxies, with large arcs and bridges joining them and the nearby galaxy NGC 3077 (e.g., Davies 1974; Yun, Ho, & Lo 1994). The large-scale velocity structure of this gas blends with the global H $\alpha$  velocity trends in M82, matching the systemic velocity and even the minor-axis velocity gradient (Cottrell 1977). The H I cloud is clearly extensive enough to replenish dust that has been destroyed by sputtering. Moreover, this massive reservoir of atomic gas should help to maintain the tenuous halo gas itself in M82, a component that is required by hydrodynamical models in order for the outflowing wind to produce observable structures (Suchkov *et al.* 1994).

### 4.3. Galactic-scale Outflow

A number of studies have concentrated on the minor axis filaments in M82. Imaging observations (e.g., Lynds & Sandage 1963; Ichikawa *et al.* 1994) have been directed toward understanding the morphology of the outflow, while spectral studies (e.g., Burbidge, Burbidge, & Rubin 1964; Heckathorn 1972; Axon & Taylor 1978; Williams, Caldwell, & Schommer 1984; Bland & Tully 1988; McKeith *et al.* 1995) have attempted to parametrize the kinematics of the filaments. The most recent observations detect split emission lines that suggest a pair of expanding bubbles or cones. The exact size and shape of the expanding structures remains a topic of some debate. Additional optical spectroscopy has measured the radial variations of line emission along the

outflow (e.g., Heckman, Armus, & Miley 1990). Ratios such as  $[\text{N II}]/\text{H}\alpha$  increase with distance from the nuclear starburst, suggesting a gradual change in the gas excitation mechanism. We now investigate these findings in light of the spatial and spectral coverage provided by our Fabry-Perot spectrophotometry.

#### 4.3.1. Optical Morphology

Optical emission line images of the M82 outflow reveal a complex distribution of radial filaments and knots along the minor axis of the galaxy. In order to examine the morphology of these filaments, R. B. Tully kindly obtained for us very deep ( $t \sim 3000$  sec)  $\text{H}\alpha$  imagery at the University of Hawaii 88-inch telescope on Mauna Kea (Fig. 8). We imaged a  $6'$  circular field, a factor of two larger than our Fabry-Perot field. The optical filaments associated with the minor axis outflow are visible across the entire field, to radial distances of at least 3.5 kpc to the north and 2 kpc to the south. This represents approximately half the extent of the soft X-ray halo (see below). The filaments are bright within a kiloparsec of the disk, particularly in the south. In these inner regions, a web of long ( $\sim 300$  pc) filaments appear distributed roughly parallel to the minor axis, amidst a “foam” of smaller emission structures. Beyond a kiloparsec in radius, the filamentary structure breaks up into fainter, more isolated clumps.

The faintness of the northern filaments is almost certainly due to obscuration by the inclined disk of the galaxy (cf. Hennessy 1996). The inclination angle of M82 is estimated to be  $81^\circ 5'$  (Lynds & Sandage 1963), such that the nearer edge of the galaxy is projected on the northwest side of the nucleus. We observe the nuclear regions of the galaxy through the southern side of the disk, and therefore expect the inner filaments to be much brighter there. If we assume a line-of-sight dimension for the optical disk equal to its linear dimension on the sky ( $\sim 11.2'$ ; de Vaucouleurs *et al.* 1991), we expect the northern outflow to be at least partially obscured to projected radii of  $\sim 0.8'$ . This is consistent with the similar morphologies of the filaments beyond this radius in the north and south in Figure 8.

Although complicated by obscuration in the north, the inner filament structure also appears to differ between the two lobes in terms of collimation. The bright inner kiloparsec of the southern lobe is relatively well confined to the minor axis, whereas the northern outflow filaments cover a much wider range of opening angle. This is seen particularly well in the  $\text{H}\alpha$  flux map from the Fabry-Perot data (Fig. 1), and is probably not an obscuration effect, but rather a difference in the physical morphology of these two lobes. One possible interpretation is that the nuclear starburst is located slightly above the galactic mid-plane. The smaller mass of covering material to the north would make collimation of an expanding wind more difficult, resulting in an almost immediate “breakout” of the wind from the disk.

Finally, we have noted that the  $[\text{N II}]/\text{H}\alpha$  ratio map and  $[\text{O III}]$  flux maps indicate that the southern outflow involves two distinct components, each originating from one of the central bright



emission regions. This may be a “limb brightening” effect as has been suggested for the pair of central emission regions themselves. This implies that the emitting filaments are distributed along the outer surface of the outflow, rather than throughout the volume. On the other hand, it is likely that the two bright central regions from which the outflow streams appear to originate are stellar “superclusters” (O’Connell *et al.* 1995) which merely happen to be physically located on either side of the kinematic center of the galaxy, from our point of view. Regardless, we do not observe emission enhancement along the outflow axis, as would be the case for a volume brightened distribution.

If we do not include emission arising within approximately  $8''$  (125 pc) of the disk, our line fits encompass an  $H\alpha$  flux of  $7.6 \times 10^{-11}$  ergs s $^{-1}$  cm $^{-2}$ . After a rough subtraction of the halo model given in the previous section, this implies a total filament luminosity  $L(H\alpha) \sim 7.6 \times 10^{40}$  ergs s $^{-1}$  (cf. Tab. 1). Assuming the filaments are completely ionized, using a case B recombination coefficient for  $T \sim 10,000$  K of  $\alpha_B = 2.59 \times 10^{-13}$  cm $^3$  s $^{-1}$  (Osterbrock 1989), and employing the outflow geometry to be discussed in Section 4.3.4 below, we calculate an rms filament density  $\langle n_e \rangle \sim 5 \cdot f^{-1/2}$  cm $^{-3}$ . A very rough estimate for the filament filling factor of  $f \sim 0.1$  would suggest a mean electron density in the filaments  $\langle n_e \rangle \sim 15$  cm $^{-3}$ , easily consistent with [S II] doublet ratios in the low-density limit throughout much of the large volume of outer filaments. This mean density implies a filament mass  $M \sim 5.8 \times 10^6 M_\odot$  distributed in a volume  $V \sim 1.1 \times 10^8$  pc $^3$ , and a kinetic energy in the ionized filaments  $KE \sim 2.1 \times 10^{55}$  ergs. These values are consistent with those first computed by Lynds & Sandage 1963,  $5.8 \times 10^6 M_\odot$  and  $2.4 \times 10^{55}$  ergs, respectively. The entire mass of outflowing gas is estimated to be a couple orders of magnitude larger (Heckman, Armus, & Miley 1990). Note that the kinetic energy in the filaments is only about one percent of the estimated input supernovae energy ( $\sim 2 \times 10^{57}$  ergs; Watson, Stanger, & Griffiths 1984).

#### 4.3.2. X-Ray Morphology

A large x-ray halo has been observed in M82 (Watson, Stanger, & Griffiths 1984; Schaaf *et al.* 1989; Tsuru *et al.* 1990; Bregman, Schulman, & Tomisaka 1995), extending at least 5–6 kiloparsecs in radius along the minor axis of the galaxy. Originally believed to be thermal emission from the hot ( $T \sim 10^7$ – $10^8$  K) gas within the outflow, current models suggest an origin in wind-shocked clouds. J.N. Bregman has kindly provided us with a recently published (Bregman, Schulman, & Tomisaka 1995) image of M82 taken with the *Röntgensatellit* (*ROSAT*; Trümper 1984) High-Resolution Imager (HRI; Pfeiffermann *et al.* 1987). The pair of  $13'$  square images with total exposure time 33.8 kiloseconds were taken in early 1991 and late 1992. The resolution is about  $5''$ .

Contours representing the *ROSAT* soft x-ray flux have been overlayed on our deep  $H\alpha$  image (Fig. 8). The morphologies are markedly similar, with specific filaments and knots clearly enhanced in both emission bands. (Note, for example, the two extensive filaments in the north, and the knots approximately 500 pc SW of the nucleus.) But in light of the more extensive distribution

of the X-rays versus the optical emission, it seems unlikely that *all* of the X-ray flux is associated with specific filaments of optical emission. Since the regions of high optical/X-ray correlation are also some of the brightest in  $H\alpha$ , these knots presumably represent density enhancements in the outflow bubbles. The large extent of the X-ray halo and close spatial correlation with the  $H\alpha$  emission suggest an interpretation in terms of shocks driven by a fast, rarefied wind plowing into denser halo gas (e.g. Sutherland, Bicknell, & Dopita 1993; Dopita & Sutherland 1996). Our observed  $H\alpha$ /X-ray luminosity ratio of  $\approx 30$  in the brightest filaments, identical to that derived by Pérez-Olea & Colina 1996, suggests a similar scenario. We defer detailed modeling of the  $H\alpha$  and soft x-ray emission to a subsequent paper, in which the shocks will be constrained by deep spectroscopy and imaging from the *Keck* and *Hubble Space Telescopes*.

#### 4.3.3. Optical Kinematics

Our Fabry-Perot observations provide velocity information across the entire outflow in M82. Two well-known features of this emission line gas should be emphasized *a priori*. First, the velocity signature of outflow is clearly observed along the minor axis in both  $H\alpha$  and  $[N\ II]$  (see Fig. 3). The well-established disk inclination angle of  $81^\circ 5'$  (Lynds & Sandage 1963) and the increased opacity toward the northern filaments clearly establishes the large-scale kinematics as arising from outflow (cf. Elvius 1972; Solinger, Morrison, & Markert 1977). Second, the optical emission lines split into two distinct velocity components in large regions along the minor axis of the galaxy. The velocity structure of the individual components, as well as the difference between them, provides convincing evidence for the presence of outflowing gas along the minor axis of M82 (Axon & Taylor 1978). Figure 9 illustrates the velocity structure of the  $H\alpha$ -emitting gas in M82, as observed in the frames of the Fabry-Perot data cube. Both minor-axis outflow lobes span velocity ranges exceeding  $v_{proj} \sim 300\text{ km s}^{-1}$ , overlapping at the systemic velocity.

We now describe our attempts to understand the complex dynamics of the outflow in M82 with the aid of kinematic models. We have extracted one-dimensional velocity cuts and synthetic two-dimensional spectra from the Fabry-Perot data cubes. These cuts have been made relative to the outflow axis, at an estimated position angle of  $\sim 150^\circ$  ( $\sim 85^\circ$  relative to the major axis of the galaxy; McKeith *et al.* 1995). While some authors have argued for a spherical wind in M82 (e.g., Seaquist & Odegard 1991), most recent models find evidence for a bipolar outflow, usually in the shape of cones with opening angles much less than  $90^\circ$ . This is borne out by our study: the line flux, splitting, and ratio maps all exhibit marked azimuthal variations indicative of an aspherical outflow morphology, strongly weighted toward the minor axis of the galaxy. Studies of the supernova distribution (e.g., Kronberg, Biermann, & Schwab 1985) and other disk observations (e.g., Achtermann & Lacy 1995) indicate that even the central injection zone is probably not spherical, but rather in the form of a flattened disk, with dimensions  $\sim 600\text{ pc}$  wide and  $\sim 200\text{ pc}$  thick.

The specific velocities predicted by Chevalier & Clegg 1985 do not agree with our observations.

An estimated supernova rate of  $0.3 \text{ yr}^{-1}$  (Rieke *et al.* 1980) yields an outflow velocity from their model of  $2000\text{--}3000 \text{ km s}^{-1}$  at the edge of the starburst injection zone. This value is several times larger than the deprojected velocities observed at optical wavelengths ( $v \sim 525\text{--}655 \text{ km s}^{-1}$ ; see below) on much larger scales. However, the extensive radio continuum halo (Seaquist, Bell, & Bignell 1985; Seaquist & Odegard 1991) could arise from synchrotron radiation due to a population of relativistic electrons, as they are transported outward in a wind at velocities in the range considered by Chevalier & Clegg. The relationship between such a wind and the slower, denser minor-axis outflow seen at optical and x-ray wavelengths remains unclear. We suspect that much of the  $\text{H}\alpha$  filamentation arises from large-scale shocks from a high-speed wind plowing into the gaseous halo and entrained disk gas. Only a small fraction of the total wind energy is encompassed by the radio halo ( $\sim 2\%$ ; Seaquist & Odegard 1991).

In modeling the bipolar outflow in M82, we model the individual line components rather than flux-weighted velocity profiles. In Figure 10, we show the velocities of line fits to the dual  $\text{H}\alpha$  components along the minor axis of the galaxy. While the northern outflow components show a relatively constant projected separation of  $\sim 300 \text{ km s}^{-1}$ , the southern region of split lines reveals an intriguing variation. Within 200 pc south of the nucleus, where the favorable inclination of the disk allows us to measure line profiles closer to the starburst, the individual components of  $\text{H}\alpha$  are separated by a much smaller velocity, comparable to our resolution ( $\sim 50 \text{ km s}^{-1}$ ). Between 200 and 500 pc from the nucleus, the components rapidly diverge, remaining at a constant separation of  $\sim 300 \text{ km s}^{-1}$  beyond 500 pc. Maps of the line component splitting reveal a separation of this order throughout the spatial extent of both lobes. Also plotted in Figure 10 are fits to the  $\text{H}\alpha$  profiles from the long-slit optical spectra of McKeith *et al.* 1995, which clearly confirms our observed minor-axis trend in the line splitting. An identical radial trend is seen in the  $[\text{N II}]$  line components along the southern outflow axis, but is not shown in the figure.

#### 4.3.4. Kinematic Models

In order to understand the intrinsic velocity structure underlying the observed kinematics, we have undertaken two separate sets of three-dimensional Monte-Carlo wind simulations: a rounded expanding bubble and a pair of cones arranged as a funnel. Although primarily geometric in nature, these models allow us to estimate the three-dimensional morphology of the outflow, as well as intrinsic gas velocities, both of which are important constraints for physical models of the wind emission mechanisms and other observational phenomena.

For our initial model, we used rounded bubble geometries, given by the spherical functions,

$$\rho = A \cos m\theta \quad -\frac{\pi}{2m} < \theta < +\frac{\pi}{2m} \quad (4)$$

$$\rho = A \cos^m \theta \quad -\frac{\pi}{2} < \theta < +\frac{\pi}{2} \quad (5)$$

(see Fig. 11a). Both functions produce a parabolic leading surface becoming conical at small

radii. The parameter  $m$  can be related to an opening angle and a Mach number in cases where the leading surface is produced in a bow shock. Truncating the bubble at inner and outer radii allows for the selection of a outflow structure with specific opening angle and radial curvature. We superimposed two alternate velocity laws upon this spatial geometry: a radial velocity vector, which corresponds physically to the case in which each gas parcel is accelerated by the flow originating at the bubble apex, or a velocity vector perpendicular to the surface of the bubble, which may be more appropriate for an expansion due to increasing heat and pressure inside the bubble, such as an inflating balloon.

We then executed a series of Monte-Carlo simulations for each velocity law, varying bubble parameters such as opening angle, inclination angle, and inner and outer truncation radii. The conclusion reached from this set of simulations is that *the rapid divergence of the velocity components in the southern outflow cannot be reproduced by a single bubble*, at least not without invoking highly contrived velocity profiles for the wind. Studies of the minor axis x-ray distribution are similarly unable to model the emission with a single bubble or cone (e.g., Suchkov *et al.* 1996).

Morphologically, one can divide the southern region of split lines into two separate velocity regimes: the region within approximately 200 pc of the nucleus, where the split line components are separated by  $\sim 50 \text{ km s}^{-1}$ , and the region beyond 500 pc radius, in which the components are separated by a much larger, but still relatively constant, projected value of  $\sim 300 \text{ km s}^{-1}$ . The inner component is not observed north of the galaxy, presumably because the split lines cannot be resolved at a sufficiently small radius due to the intervening inclined disk of the galaxy. Note that the  $\text{H}\alpha$  and  $[\text{N II}]$  flux maps (Fig. 1) also suggest the presence of two distinct regions, as the line flux drops sharply at the same radius at which the velocity components rapidly separate ( $\sim 500 \text{ pc}$ ).

We therefore performed another set of Monte-Carlo simulations, this time using a double cone geometry, given by the cylindrical function

$$r = \begin{cases} \kappa_1(z - z_{01}), & 0 < z < 350 \text{ pc} \\ \kappa_2(z - z_{02}), & 350 < z < 800 \text{ pc} \end{cases} \quad (6)$$

(see Fig. 11*b*). The  $\kappa$  parameters determine the opening angles of the cones, while the  $z_0$  parameters control the radial extent of the cones through truncation. Again, we superimposed both radial and normal (i.e., perpendicular) velocity laws, but determined in the end that a velocity vector tangential to the cone surfaces provided the best match to the observations and was most easily understood physically, in terms of material entrained by the high-velocity wind. An additional parameter was used to smooth the abrupt projected velocity transition where the two cones meet (at  $z = 350 \text{ pc}$ ).

After performing simulations over a range of cone sizes, inclination angles, opening angles, and velocity laws, we derived the final model shown in Figure 12. Parameters of the cones which best fit the observations are given in Table 3. The inner “cone” is almost a cylinder of radius equal to the injection zone ( $r \sim 200 \text{ pc}$ ), with a small, but non-zero, opening angle. The outer

cone has an opening angle of approximately  $25^\circ$ , in relative agreement with the “small” opening angle models of Bland & Tully 1988 and McKeith *et al.* 1995. Models in the “large” opening angle regime (e.g.,  $60^\circ$ ; Heckman, Armus, & Miley 1990) do not match the observations, requiring excessively low intrinsic velocities and a larger projected spatial extent for the outflow region (see Fig. 12a). A large opening angle for the primary outflow cone also produces substantially skewed Doppler ellipses in spectra perpendicular to the outflow axis. This effect is due to the slit cutting through the back and front of the cone at different nuclear radii, and is not observed in our synthetic spectra (see Figs. 12c and 12d).

The inner and outer cones are inclined toward the observer by  $\sim 5^\circ$  and  $\sim 15^\circ$ , respectively, roughly aligning the back sides of the two cones (see Fig. 11b). This is required to explain the lack of a sharp velocity gradient in the low-velocity component (LVC) at a radius of 350 pc, as is observed in the high-velocity component (HVC). In addition, since the LVC exhibits small but non-zero projected velocities, the back sides of the cones must be at a slight angle to the plane of the sky. These inclination angles agree with previous estimates (e.g., Burbidge, Burbidge, & Rubin 1964; Hennessy 1996). While the observed velocities of the HVC could be duplicated with smaller cone opening angles and a larger inclination, the low velocities of the LVC require small inclination angles.

Initial attempts to model the kinematics of the outflow with a constant velocity law, i.e., using only the simple double-cone geometry to reproduce the observed velocity structure, were not successful. Figure 10 illustrates that both velocity components in the south and north exhibit non-zero slopes in the position-velocity plot. This can be understood as either a continuous change in the intrinsic gas velocity or as a change in the projected velocity through a continuous change in the outflow cone geometry. The latter case implies that both sides of the outer cone are constantly bending toward the observer, producing a slowly increasing projected velocity with radius. A gradually increasing intrinsic wind velocity is probably necessary as well, and can be understood from a physical standpoint. Buoyancy effects in the hot wind from the decreasing disk density with scale height, decreasing wind densities from the lack of collimation at larger radii, and other effects contribute to produce wind velocities that increase with radius in standard galactic wind models (e.g., Chevalier & Clegg 1985; Suchkov *et al.* 1994). After testing a number of stronger power-law expressions for the gas velocity dependence on radius, we finally chose the simple linear model given in Table 3. Together with a constant cone opening angle, this intrinsic velocity structure produces linear projected velocity gradients that correspond well to those observed in Figure 10. The intrinsic velocities of the gas range from  $525 \text{ km s}^{-1}$  near the nucleus to  $655 \text{ km s}^{-1}$  at a radius of 1 kpc. These velocities are comparable to the escape velocity for M82 (see Table 1), implying that the most distant entrained filaments are not bound to the galaxy. This conclusion is also supported by the large radial extent of the fast wind itself, as seen in soft X-rays, along the minor axis.

Just as the outflow cones are not aligned with the minor axis of the galaxy along the line of sight, neither are they aligned in the plane of the sky. The region of split  $\text{H}\alpha$  lines constitutes

a cone on the sky with the expected opening angle of  $\sim 25^\circ$ , but with a position angle of  $\sim 165^\circ$ , approximately  $15^\circ$  greater than what the literature (e.g., McKeith *et al.* 1995) had previously defined as the “outflow axis.” The cone axis is rotated  $\sim 100^\circ$  from the major axis of the galaxy, and places the eastern edge of the cone almost directly parallel to the minor axis. In fact, Figure 12a illustrates that this eastern edge is quite pronounced, both in the split emission lines and in the  $H\alpha$  flux observed from the inner collimated zone. This suggests that the tilting of the outflow cones in the plane of the sky has been produced by a relative density enhancement in the eastern lower halo which maintains collimation of the wind even as it fans out toward the west and toward the observer.

While the large outflow cones appear to originate east of the galaxy’s minor axis, a small region of split lines is also observed on the western edge of the collimated zone, approximately 300 pc from the nucleus. The morphology of the  $H\alpha$  and [O III] flux maps (Figs. 1 and 2) indicates that this region constitutes a small bubble on the side of the larger outflow structure. We clearly see an enhanced rim of  $H\alpha$  emission around the bubble, and split lines within it.

Recalling again the identification of two outflow “streams” in the [O III] flux map and the [N II]/ $H\alpha$  ratio map (Figs. 2 and 4), one might expect a more substantial outflow from the western half of the nucleus, or at least a more centrally-positioned outflow cone. However, it appears that gas densities on the western side of the lower halo are substantial enough to keep the western stream from expanding into a cone. The stream appears to bend toward the west in the [O III] flux map (Fig. 2), and the only expanding structure that we observe is the one small bubble.

But at larger radii, the ambient density toward the west must drop relative to the eastern side. While the outflow remains tightly confined to the east, even beyond the collimated zone, certain Fabry-Perot maps show evidence of variations in the western side of the outer outflow cone, suggesting a more azimuthally-extended morphology there, e.g., break-out into a less dense region. For example, the  $H\alpha$  velocity map (Fig. 3) reveals high velocity clumps at radii of  $\sim 1$  kpc that are distributed westward from the sharp eastern edge over almost  $90^\circ$  in azimuth. These clumps are clearly associated with the outflow, and can also be seen as the blue-shifted emission just west of the split line region in our most distant outflow cut, Figure 12d. The fact that this gas exhibits smaller velocities in panel *c* of this figure illustrates that kinematical effects from disk rotation are greater closer to the disk. In contrast, the emission immediately east of the split line region lies at effectively the same velocity in both panels *c* and *d* of Figure 12, as this coincides with the sharp collimating edge on that side of the outflow. The spatial structure of the  $H\alpha$  velocity map (like that published in Heckathorn 1972) also suggests the presence of rotating disk material that has been entrained and gradually diverted to the outflow.

To summarize, the inner 350 pc of the outflow constitutes a flow down a pipe. The outflow is collimated, presumably by ambient and entrained disk material, and highly inclined to our line of sight, such that the observed radial component of the flow velocity is only  $\sim 50$  km s $^{-1}$ . Beyond 350 pc, however, the collimation weakens and the outflow expands rapidly as a cone of emission

with an opening angle of  $25^\circ$  and a projected front-to-back velocity separation of approximately  $300 \text{ km s}^{-1}$ . This expansion is preferentially toward the west and toward the observer. A linearly increasing intrinsic gas velocity with an initial value of  $525 \text{ km s}^{-1}$  and a gradient of  $0.13 \text{ km s}^{-1} \text{ pc}^{-1}$  matches the observations well out to a radius of a kiloparsec.

The line-splitting phenomenon indicates that the  $\text{H}\alpha$ -emitting filaments are produced on the surface of the outflow cones, at the interface between the wind and the ambient halo material. In addition to the minor axis velocity structure, this model explains the increased flux within the collimated region (see Fig. 12a) as a result of an elevated density with respect to the outer expanding cone ( $\mathcal{F} \propto n_e^2$ ). An increased density in the innermost regions has also been indicated observationally by the “filling in” of the line profiles at those radii (e.g., McKeith *et al.* 1995).

While the inner bubble has an extremely small opening angle, we find that an outer cone of opening angle  $\sim 20^\circ$ – $30^\circ$  fits the data most closely. This range agrees well with the “small” opening angle values found by other authors (e.g.,  $\sim 30^\circ$ ; McKeith *et al.* 1995). Our observations do not support the “large” opening angle regime (e.g.,  $\sim 60^\circ$ ; e.g., Heckman, Armus, & Miley 1990).

#### 4.3.5. Comparison of Kinematic with Hydrodynamic Models

Striking support for the two-zone model is obtained from a comparison with recent hydrodynamic outflow models. Initial two-dimensional simulations (e.g., Tomisaka & Ikeuchi 1988) proposed an evolution of the outflow which included collimation of the flow at early stages by disk material, subsequent breakout of the confined flow along the minor axis, and eventual extension of the hot wind material up to a few kpc from the nucleus.

More recent simulations (Tomisaka & Bregman 1993; Suchkov *et al.* 1994; Suchkov *et al.* 1996) include a separate corotating halo component and are able to reproduce much of the observed morphology through the interactions of the wind with the disk and halo. These simulations show that the outflow entrains disk gas around itself, dragging the cooler, denser material up to a couple of kiloparsecs above the plane of the galaxy (e.g., see Fig. 6 in Suchkov *et al.* 1994). The regions of densest entrained disk material, near the base of the outflow, serve to collimate the outflow beyond the height of the disk itself. The scale height of this collimation in the simulations is similar to that seen in our observations,  $\sim 500 \text{ pc}$ . The “fingers” of disk material entrained to heights above the collimated zone can be identified with the optical emission line filaments we observe on the outer walls of the outflow cone. This entrained gas has also been observed at molecular wavelengths (e.g., Stark & Carlson 1984; Nakai *et al.* 1987; Sofue *et al.* 1990). Within the collimated region, the simulations show that both the wind and the confining walls are at their densest, consistent with the observed increased levels of optical emission. Finally, it should be noted that a recent analysis of the minor-axis X-ray distribution implies a partially confined outflow of this gas as well, within 1.6 kpc of the disk (Bregman, Schulman, & Tomisaka 1995).

#### 4.3.6. Comparison of Optical and X-ray Observations

A number of authors have observed an extensive nebula of soft X-ray emission along the minor axis of M82 (e.g., Watson, Stanger, & Griffiths 1984; Schaaf *et al.* 1989; Tsuru *et al.* 1990; Bregman, Schulman, & Tomisaka 1995). The initial interpretation was that these are thermal X-rays, produced by the hot ( $T \sim 10^7$  K) gas in the outflow. The optical line emission must then arise from the cooler boundary layer of the wind, where the hot gas interacts with entrained disk and ambient halo material. Such a hot gas would not be gravitationally bound to the galaxy and could easily expand to the the observed radial distances of 5–6 kpc (Bregman, Schulman, & Tomisaka 1995) in the estimated age of the starburst ( $t \sim 5 \times 10^7$  yr; Rieke *et al.* 1980; Doane & Mathews 1993). Recent ASCA observations (Tsuru *et al.* 1994; Moran & Lehnert 1997) find three temperature components in this wind, with more extended softer components, confirming that the hot wind is cooling as it expands.

Recent hydrodynamic simulations and studies of the x-ray halo spatial distribution have cast doubt on this interpretation, however. Current hydrodynamic simulations (Tomisaka & Bregman 1993; Suchkov *et al.* 1994) derive gas temperatures an order of magnitude larger than earlier estimates (e.g., Watson, Stanger, & Griffiths 1984). This  $10^8$  K gas does not emit as strongly in the X-ray bands, producing insufficient soft and hard X-rays to account for the observations. Even Chevalier & Clegg 1985 admit that the density falls too rapidly in their simple model to account for the x-ray photons as thermal. X-ray spectral studies derive a range of thermal gas temperatures and suggest alternative emission mechanisms (Fabbiano 1988; Schaaf *et al.* 1989; Strickland, Ponman, & Stevens 1996). Finally, correlations between our deep H $\alpha$  imaging and Fabry-Perot observations and high-resolution *ROSAT* imagery support a non-thermal origin for at least a portion of the minor-axis x-ray emission.

Figure 13 compares the spatial distribution of soft X-rays observed by *ROSAT* with our Fabry-Perot H $\alpha$  flux map. As was evident at larger radii in the comparison with the deep H $\alpha$  imagery (Fig. 8), the X-rays and optical line emission are clearly correlated. On large scales, the minor-axis x-ray flux drops at a radius of approximately 500 pc from the nucleus, as does the H $\alpha$  emission. But also on scales as small as 10 pixels (150 pc), the x-ray and optical emission appears well correlated. This implies that soft X-rays are being produced in regions very close to those which are producing H $\alpha$  emission, a situation which is very difficult to understand in terms of a thermal emission mechanism.

These observations lend support to the x-ray emission mechanism suggested by several authors (e.g., Chevalier & Clegg 1985; Suchkov *et al.* 1994; Strickland, Ponman, & Stevens 1996): the soft X-rays arise from shocked disk and halo “clouds.” This shocked gas can produce both the observed x-ray and optical emission, accounting for the spatial correlation in Figure 13. A hybrid model seems necessary in which the higher gas temperatures and densities near the nucleus create a region dominated by shocks at interfaces with disk and halo gas clouds, while the cooler temperatures and lower densities at larger radii produce a decrease in optical emission and an



increase in thermally-emitted x-rays. A comparison of the scale lengths of the  $H\alpha$  and x-ray emission along the minor axis confirms the more extended nature of the x-ray component: the  $H\alpha$  surface brightness along the minor axis is fit well by an exponential function, with a scale length of  $\sim 250$  pc. For the most distant  $H\alpha$  emission ( $r \sim 1$  kpc), this exponential can be approximated by a power law of slope  $-2$ , essentially the same power law exponent measured for the X-rays at a comparable radius (Bregman, Schulman, & Tomisaka 1995). Beyond this radius, the optical surface brightness falls more rapidly than does the x-ray surface brightness.

Recent detailed modeling of the x-ray emission (Bregman, Schulman, & Tomisaka 1995) suggests a temperature at large radii of only  $\sim 2 \times 10^6$  K, implying an increasing role for thermal emission with radius. Similarly, hydrodynamic simulations find that the majority of the wind mass must be accumulated near the starburst region, not from evaporating halo clouds (Suchkov *et al.* 1996). It should be noted, however, that observations with the Ginga x-ray satellite have made the startling discovery of faint x-ray emission extending several *tens* of kiloparsecs from M82 (Tsuru *et al.* 1990). Hydrodynamic simulations have modeled this emission as shock-excited in nature, assuming that the outflow is much older,  $\sim 5 \times 10^7$  years (Tomisaka & Bregman 1993). Although this observation has yet to be confirmed, the rapid radial decrease in the wind pressure and density could propagate the wind shock to large distances from its starburst origins.

The true importance of shocks versus thermal emission can be estimated from optical line diagnostics, at least in the inner regions of the M82 outflow. As was pointed out in Section 3, the flux-weighted  $[N II]/H\alpha$  ratio from the Fabry-Perot data is highly uniform and low in the inner kiloparsec of the outflow; values of 0.3–0.6 are typical. However, we must be careful to use line ratios for individual kinematic components when drawing conclusions regarding the physics of the gas, especially when the components have been modeled as distinct physical regions. The  $[N II]/H\alpha$  line ratio of the individual components reveals a similar low value across the spatial extent of split lines, except in the inner collimated zone, where a higher  $[N II]/H\alpha$  ratio is seen ( $\sim 1.0$ ), particularly in the low-velocity component. Although we were unable to resolve separate components in the  $[O III]$  observations, we note that the  $[O III]/H\alpha$  ratio exhibits a strong radial gradient, unlike the  $[N II]/H\alpha$  ratio. The  $[O III]/H\alpha$  ratio increases from a value of approximately 0.03 at the center to 0.08 at a distance of  $\sim 750$  pc.

In order to investigate the importance of shock excitation for the optical filaments, we have compared the observed emission line ratios from the Fabry-Perot data with the standard emission-line galaxy diagnostic diagrams of Veilleux & Osterbrock 1987. Although the small number of emission line diagnostics at our disposal limits our analysis, we can nevertheless make a rough assessment of the influence of shocks using the  $[O III]/H\beta$  versus  $[N II]/H\alpha$  diagnostic diagram (Fig. 14; from Fig. 1 of Veilleux & Osterbrock 1987). Using an  $H\beta/H\alpha$  ratio of 0.25 for the outflow gas (Heckman, Armus, & Miley 1990), we see that the emission line ratios from the southern wind lobe of M82 rest in the region of the diagram for starburst galaxies, as expected. The ratios are comparable to those for most cooler H II regions and H II region models. This immediately suggests an emission mechanism such as photoionization for the filaments, particularly

near the nucleus, where the  $[\text{O III}]/\text{H}\alpha$  ratio is lower. As we move out in radius, however, shocks appear to become more important as an excitation mechanism, as the increasing  $[\text{O III}]/\text{H}\alpha$  ratio drives the locus in Figure 14 toward the region for non-thermally powered AGN.

In order to more directly interpret our emission line fluxes in light of a shock mechanism, we have also compared the observed line ratios with a recent set of high-velocity shock models (Dopita & Sutherland 1995). These models have been computed for shocks in the velocity range of  $150\text{--}500 \text{ km s}^{-1}$ ; the deprojected gas velocity of the wind in M82 is estimated to be at the upper end of this range. Again using an  $\text{H}\beta/\text{H}\alpha$  ratio of 0.25 for the outflow gas (Heckman, Armus, & Miley 1990), a comparison with the  $[\text{O III}]/\text{H}\beta$  versus  $[\text{N II}]/\text{H}\alpha$  diagnostic diagram (Fig. 15; from Fig. 2b of Dopita & Sutherland 1995) shows that it is unlikely that the observed emission line flux from the inner outflow filaments arises entirely from shocks. There is simply not enough  $[\text{O III}]$  emission observed in the inner kiloparsec of the M82 outflow. However, the increasing  $[\text{O III}]/\text{H}\alpha$  ratio with distance from the nucleus suggests that shocks probably become important at larger radii, just as suggested by the observational diagnostic diagrams (Veilleux & Osterbrock 1987). Longslit optical observations have also reached the conclusion that the line ratios become more shock-like with increasing distance from the starburst (e.g., Heckman, Armus, & Miley 1990), although this has often not included analysis of individual velocity components.

Additional support for a photoionization mechanism for the inner optical filaments is provided by studies of the diffuse ionized medium (DIM) in NGC 891. In that galaxy, which has no outflow or other obvious sources of shock ionization, photoionization models have been used to understand the variation of line ratios with height above the disk plane. These models show that the  $[\text{N II}]/\text{H}\alpha$  ratio gradually decreases as the ionization parameter (the ratio of ionizing photons to gas density) increases. In contrast, the  $[\text{O III}]/\text{H}\alpha$  ratio should increase rapidly with ionization parameter (Sokolowski 1992). Regardless of the presence of shocks then, the low value of  $[\text{N II}]/\text{H}\alpha$  and the gradually increasing value of  $[\text{O III}]/\text{H}\alpha$  in the innermost filaments of M82 can be understood as the result of a gradual drop in filament density, relative to the number of ionizing photons from the starburst. In the outer filaments, however, the  $[\text{N II}]/\text{H}\alpha$  ratio begins to increase, presumably as a result of dilution of the radiation field in the expanding uncollimated bubble, as well as perhaps an increasing influence of shocks.

Recent studies of the influence of halo dust on these line ratio trends in NGC 891 (Ferrara *et al.* 1996) point out that the  $[\text{N II}]/\text{H}\alpha$  ratio may appear artificially low near the disk due to dilution by scattered radiation from disk H II regions. This suggests that the low  $[\text{N II}]/\text{H}\alpha$  ratios for the inner filaments in M82 may be due in part to higher dust densities in the inner halo, scattering disk radiation from the nuclear starburst. This proposition corresponds well with the high levels of polarization detected from the filaments and the exponential nature of the observed halo, although the observed polarization levels in M82 ( $\sim 10\text{--}15\%$ ) are much higher than those modeled in NGC 891 ( $\sim 1\text{--}2\%$ ).

Based upon these comparisons and our geometric models, we propose that the optical emission

from the inner kiloparsec of the M82 filament network is, at least partially, due to photoionization of the sides of the cavity created by the outflow. The hot gas in the wind itself would be quite transparent to the UV ionizing photons from the starburst region, allowing the entrained disk and halo gas to be illuminated directly. The tipped geometry of the outflow cones probably places the systemic side of each cone more directly in the path of the photoionizing radiation from the central starburst, explaining the higher fluxes seen in the low-velocity components of the wind. However, small regions of higher  $[\text{N II}]/\text{H}\alpha$  ratios in the individual velocity components suggest that a complex combination of shock and photoionization is probably required in the violent collimated zone, where the disk gas is being entrained and drawn upward by the hot wind just as it leaves the luminous starburst region. Although our small field of view and sensitivity limits restrict our analysis of the more extended optical filaments, we confirm a trend toward more shock-like line emission in the outer regions of the outflow.

#### 4.3.7. Comparison with UV Observations

The inner regions of the outflow in M82 have been detected in UV images taken with the *Ultraviolet Imaging Telescope* (UIT; Stecher *et al.* 1992). Figure 16 compares our deep  $\text{H}\alpha$  image with the UV image observed in the  $2490\text{\AA}$  band by the *UIT*. The southern outflow is clearly evident in ultraviolet emission, out to at least a kiloparsec. The northern outflow is only barely visible in the *UIT* data, presumably because of the high disk extinction at ultraviolet wavelengths. The projected morphology of the southern UV outflow is similar to that at  $\text{H}\alpha$  wavelengths, consisting of a relatively smooth, broad fan of emission. The ratio of the  $\text{H}\alpha$  and UV surface brightnesses (each in units of  $\text{ergs s}^{-1} \text{ cm}^{-2} \text{ arcsec}^{-2} \text{ \AA}^{-1}$ ) in the outflow region is  $\sim 8.8$  (Hennessy 1996).

Previous analyses of the *UIT* data (Maran *et al.* 1991; Hennessy 1993), as well as earlier balloon observations (Courvoisier *et al.* 1990; Blecha *et al.* 1990) have interpreted the minor-axis ultraviolet emission in M82 in terms of dust scattering of photons from the nuclear starburst by particles in the outflow. It has been suggested that filamentary structures can be seen in the *UIT* data (Maran *et al.* 1991), presumably because the higher relative densities in the filaments enhance scattering in those regions. The spatial distribution of the UV emission does not correlate well with the  $\text{H}\alpha$ , X-ray, radio continuum, or IR morphologies, although this may be due to variations in opacity (Courvoisier *et al.* 1990). One difficulty with the scattering picture for the production of the southern UV outflow is the surprising non-detection of emission in the *UIT*  $1600\text{\AA}$  far-ultraviolet (FUV) band (Hennessy 1993). The naive expectation for Rayleigh scattering would be to expect increased scattered flux at shorter wavelengths, even in the presence of substantial extinction along the line of sight. Ultraviolet observations of reflection nebula (e.g., Calzetti *et al.* 1995) and starburst galaxies (Calzetti, Kinney, & Storchi-Bergmann 1994) derive extinction curves that confirm this expectation.

An alternative explanation for the UV light is “two photon” continuum emission from ionized

gas within the optical filaments. This emission arises from the spontaneous two-photon decay of the  $2^2S$  level of H I and is commonly seen in AGN and regions of low-density ionized gas. The spectral distribution of two-photon emission is symmetric, in photons per frequency interval, about a peak at  $2431\text{\AA}$  (Osterbrock 1989), very close to the *UIT*  $2490\text{\AA}$  band. Unlike the scattering function, two-photon flux decreases ( $\sim \lambda^{-1}$ ) toward shorter wavelengths (see also Hennessy 1996). Preliminary analysis of the [S II]  $\lambda\lambda 6719, 6731$  lines in optical spectra of the outflow from the *Keck* telescope confirm previous studies (e.g., Rodriguez & Chaisson 1980; Houck *et al.* 1984; Heckman, Armus, & Miley 1990) that the inner filament densities rarely exceed  $500\text{ cm}^{-3}$ . As this is significantly below the critical density at which collisional effects influence the intensity of two-photon emission ( $n_e \sim 10^4\text{ cm}^{-3}$ ; Osterbrock 1989), we may anticipate the filamentary nature of the outflow in the UV imagery.

The observed  $H\beta/H\alpha$  ratio of 0.25 for the outflow gas (Heckman, Armus, & Miley 1990) implies an  $H\beta/\text{UV}$  ratio of  $\sim 2.2$ . This is approximately a factor of ten greater than the ratio of  $H\beta$  to two-photon flux predicted by photoionization models ( $\sim 0.1$ ; Dopita, Binette, & Schwartz 1982; Dopita 1997), suggesting the presence of 2.5 mag more extinction at  $2500\text{\AA}$ . The observed extinction law for starburst galaxies (Calzetti, Kinney, & Storchi-Bergmann 1994; Fig. 5), combined with the observed  $H\alpha$  extinction factor of 1.8 in the outflow (Heckman, Armus, & Miley 1990) indicates that this level of obscuration is entirely reasonable. Shock-induced two-photon emission is almost certainly ruled out, as it would require extinction by a factor of  $\sim 4$  to match the observed UV intensity, well above the value observed in the outflow regions. Spectral observations near the Balmer limit,  $\sim 3650\text{\AA}$ , where the two-photon continuum emission is enhanced relative to line emission, could be useful for determining the importance of this mechanism.

## 5. Conclusions

It is widely recognized that M82 is the prototype of galactic wind systems. Most models have concentrated on explaining measurements taken along isolated position angles close to the galaxy’s minor axis. However, our new study has shown that the filamentary system associated with the outflow is highly complex. Our simplest kinematic model requires at least two discrete structures for each side of the galaxy. The filaments are distributed in a network over these surfaces. More surprisingly, the axes of the outflows on either side of the disk are aligned neither with each other nor with the spin axis of the disk. The gas excitation suggests that stellar ionization dominates close to the disk with increased dominance of shock excitation further along the outflow. The clearest signature of the biconic outflow geometry is seen in the line ratio maps which suggest that radiation is escaping from the disk along a channel excavated by the hot rarefied wind. We find evidence for a smooth line-emitting halo which we associate with the linearly polarized halo seen in broadband studies. We have observed a warm ionized medium throughout the inclined spiral disk.

In our view, the most pressing issue is an explanation of the emission-line spectropolarimetry.

We strongly urge that these observations are repeated to deeper levels, at least to the point where the diffuse line-emitting halo is detected. Observations which *only* detect the bright filaments cannot remove the contribution from the halo along the line of sight.

The disk-halo interaction in galaxies is a fundamental topic in its own right (Bloemen 1990). We suggest that M82 may provide the best observational constraints on fountain flows (e.g., Shapiro & Benjamin 1991) once the origin of the filaments is fully understood. What happens to the entrained material that is lifted into the galactic halo? What is the relationship between the relativistic electron halo, the wind filaments, and the diffuse line-emitting halo? We suspect that answers can only come from future observations of x-ray, radio and millimeter emission at a resolution and sensitivity comparable to the present study.

Funding for this research was provided by the office of the Dean of Natural Sciences at Rice University, the Texas Space Grant Consortium, and the Sigma Xi Research Society. Additional funding was provided by AURA/STScI (grant GO-4382.01.92A), the National Science Foundation (grant AST 88-18900), the William F. Marlar Foundation, the National Optical Astronomy Observatories (NOAO), and Mr. and Mrs. William Gordon. This research was performed in partial fulfillment of the Ph.D. degree at Rice University. JBH acknowledges a Fullam Award from the Dudley Observatory.

We thank Drs. Reginald J. Dufour, Patrick M. Hartigan, Jon C. Weisheit, C. R. O'Dell, and Sylvain Veilleux for enlightening discussions of the material contained herein. Special thanks is due Drs. Joel Bregman and Brent Tully for providing the *ROSAT* and deep  $H\alpha$  imagery, respectively, and Drs. Geoff Bicknell and Michael Dopita for their assistance with the stellar wind equations and high-velocity shock models, respectively.

This research has made use of the NASA/IPAC Extragalactic Database (NED) which is operated by the Jet Propulsion Laboratory, Caltech, under contract with the National Aeronautics and Space Administration. The Astrophysics Science Information and Abstract Service (ASIAS), administered by the Astrophysics Data System (ADS), was also used. Color versions of several figures in this paper are available from the authors.

## REFERENCES

- Achtermann, J. M., & Lacy, J. H. 1995, *ApJ*, 439, 163
- Arav, N., & Li, Z.-Y. 1994, *ApJ*, 427, 700
- Arav, N., Li, Z.-Y., & Begelman, M. C. 1994, *ApJ*, 432, 62
- Armus, L., Heckman, T. M., & Miley, G. K. 1990, *ApJ*, 364, 471
- Armus, L., Heckman, T. M., Weaver, K. A., & Lehnert, M. D. 1995, *ApJ*, 445, 666
- Axon, D. J., & Taylor, K. 1978, *Nature*, 274, 37
- Baum, S. A., O’Dea, C. P., Dallacassa, D., De Bruyn, A. G., & Pedlar, A. 1993, *ApJ*, 419, 553
- Beck, S. C., Lacy, J. H., Baas, F., & Townes, C. H. 1978, *ApJ*, 226, 545
- Becklin, E. E., Gatley, I., & Werner, M. W. 1982, *ApJ*, 258, 135
- Bettoni, D., & Galletta, G. 1982, *A&A*, 113, 344
- Bland, J., & Tully, R. B. 1988, *Nature*, 334, 43
- Bland, J., & Tully, R. B. 1989, *AJ*, 98, 723
- Bland-Hawthorn, J., Sokolowski, J., & Cecil, G. 1991, *ApJ*, 375, 78
- Bland-Hawthorn, J., Shopbell, P. L., Veilleux, S., & Jones, D. H. 1997, in preparation
- Blecha, A., Golay, M., Huguenin, D., Reichen, D., & Bersier, D. 1990, *A&A*, 233, L9
- Bloemen, H., The Interstellar Disk-Halo Connection in Galaxies, IAU Symp. 144 (Kluwer Academic Publishers: Dordrecht)
- Boer, B., Schulz, H., & Keel, W. C. 1992, *A&A*, 260, 67
- Bregman, J. N., Schulman, E., & Tomisaka, K. 1995, *ApJ*, 439, 155
- Burbidge, E. M., Burbidge, G. R., & Rubin, V. C. 1964, *ApJ*, 140, 942
- Calzetti, D., Kinney, A. L., & Storch-Bergmann, T. 1994, *ApJ*, 429, 582
- Calzetti, D., Bohlin, R. C., Gordon, K. D., Witt, A. N., & Bianchi, L. 1995, *ApJ*, 446, L97
- Castles, J., McKeith, C. D., & Greve, A. 1991, *Vistas in Astr.*, 34, 187
- Chevalier, R. A., & Clegg, A. W. 1985, *Nature*, 317, 44
- Christopoulou, P. E., Holloway, A. J., Steffen, W., Mundell, C. G., Thean, A. H. C., Goudis, C. D., Meaburn, J., & Pedlar, A. 1997, *MNRAS*, 284, 385

- Colbert, E. J. M., Baum, S. A., Gallimore, J. F., O’Dea, C. P., Lehnert, M. D., Tsvetanov, Z. I., Mulchaey, J. S., & Caganoff, S. 1996, *ApJS*, 105, 75
- Colbert, E. J. M., Baum, S. A., Gallimore, J. F., O’Dea, C. P., & Christensen, J. A. 1996, *ApJ*, 467, 551
- Colina, L., & Pérez-Olea, D. E. 1992, *MNRAS*, 259, 709
- Cottrell, G. A. 1997, *MNRAS*, 178, 577
- Courvoisier, T. J.-L., Reichen, M., Blecha, A., Golay, M., & Huguenin, D. 1990, *A&A*, 238, 63
- Crawford, C. S., & Fabian, A. C. 1992, *MNRAS*, 259, 265
- Dahlem, M., Petr, M. G., Lehnert, M. D., Heckman, T. M., & Ehle, M. 1997, *A&A*, 320, 731
- Davies, R. D. 1974, in *The Formation and Dynamics of Galaxies*, ed. J. R. Shakeshaft, IAU Symp. 58 (Kluwer Academic Publishers: Dordrecht), p. 119
- de Vaucouleurs, G., de Vaucouleurs, A., Corwin, Jr., H. G., Buta, R. J., Paturel, G., & Fouqué, P. 1991, *Third Reference Catalogue of Bright Galaxies* (Springer-Verlag: New York)
- Doane, J. S. 1993, PhD Thesis, University of California, Santa Cruz, California
- Doane, J. S., & Mathews, W. G. 1993, *ApJ*, 419, 573
- Donahue, M., & Voit, G. M. 1991, *ApJ*, 381, 361
- Dopita, M. A. 1997, private communication
- Dopita, M. A., Binette, L., & Schwartz, R. D. 1982, *ApJ*, 261, 183
- Dopita, M. A., & Sutherland, R. S. 1995, *ApJ*, 455, 468
- Dopita, M. A., & Sutherland, R. S. 1996, *ApJS*, 102, 161
- Duffy, P. B., Erickson, E. F., Haas, M. R., & Houck, J. R. 1987, *ApJ*, 315, 68
- Elvius, A. 1969, *Lick Obs. Bull.*, 7, 117
- Elvius, A. 1972, *A&A*, 19, 193
- Evans, I. N., & Dopita, M. A. 1985, *ApJS*, 58, 125
- Fabbiano, G., Heckman, T., & Keel, W. C. 1990, *ApJ*, 355, 442
- Fabbiano, G., & Trinchieri, G. 1984, *ApJ*, 286, 491
- Fabbiano, G. 1988, *ApJ*, 330, 672

- Ferrara, A., Bianchi, S., Dettmar, R.-J., & Giovanardi, C. 1996, *ApJ*, 467, L69
- Ferrara, A. 1997, in *The Local Bubble and Beyond*, IAU Symp. 166 (Springer-Verlag: New York), preprint
- Forbes, D. A., Boisson, C., & Ward, M. J. 1992, *MNRAS*, 259, 293
- Ford, H. C., Crane, P. C., Jacoby, G. H., Lawrie, D. G., & van der Hulst, J. M. 1985, *ApJ*, 293, 132
- Freedman, W. L., Hughes, S. M., Madore, B. F., Mould, J. R., Lee, M. G., Stetson, P., Kennicutt, R. C., Turner, A., Ferrarese, L., Ford, H., Graham, J. A., Hill, R., Hoessel, J. G., Huchra, J., & Illingworth, W. 1994, *ApJ*, 427, 628
- Gaffney, N. I., & Lester, D. F. 1992, *ApJ*, 394, 139
- Goad, J. W., & Gallagher, J. S. 1985, *ApJ*, 297, 98
- Hamilton, D., & Keel, W. C. 1987, *ApJ*, 321, 211
- Hayes, D. S. 1970, *ApJ*, 159, 165
- Hayes, D. S., & Latham, D. W. 1975, *ApJ*, 197, 593
- Heckathorn, H. M. 1972, *ApJ*, 173, 501
- Heckman, T. M., Armus, L., & Miley, G. K. 1990, *ApJS*, 74, 833
- Heckman, T. M., Dahlem, M., Lehnert, M. D., Fabbiano, G. A., Gilmore, D., & Waller, W. H. 1995, *ApJ*, 448, 98
- Hennessy, G. S. 1993, *BAAS*, 25, 1328
- Hennessy, G. S. 1996, PhD Thesis, University of Virginia, Charlottesville, Virginia
- Houck, J. R., Shure, M. A., Gull, G. E., & Herter, T. 1984, *ApJ*, 287, L11
- Huang, Z. P., Thuan, T. X., Chevalier, R. A., Condon, J. J., & Yin, Q. F. 1994, *ApJ*, 424, 114
- Hunter, D. A., & Gallagher III, J. S. 1990, *ApJ*, 362, 480
- Ichikawa, T., van Driel, W., Aoki, T., Soyano, T., Tarusawa, K., & Yoshida, S. 1994, *ApJ*, 433, 645
- Jones, A. P., Tielens, A. G. G. M., & Hollenbach, D. J. 1996, *ApJ*, 469, 740
- Keel, W. 1983, *ApJ*, 269, 466
- Kobulnicky, H. A., & Skillman, E. D. 1996, *ApJ*, 471, 211



- Koo, B.-C., & McKee, C. F. 1992, *ApJ*, 388, 93
- Koo, B.-C., & McKee, C. F. 1992, *ApJ*, 388, 103
- Krabbe, A., Colina, L., Thatte, N., & Kroker, H. 1997, *ApJ*, 476, 98
- Kronberg, P. P., Biermann, P., & Schwab, F. R. 1985, *ApJ*, 291, 693
- Lehnert, M. D., & Heckman, T. M. 1995, *ApJS*, 97, 89
- Lehnert, M. D., & Heckman, T. M. 1996, *ApJ*, 462, 651
- Lípari, S., Colina, L., & Macchetto, F. 1994, *ApJ*, 427, 174
- Loiseau, N., Nakai, N., Sofue, Y., Wielebinski, R., Reuter, H.-P., & Klein, U. 1990, *A&A*, 228, 331
- Lynds, C. R., & Sandage, A. R. 1963, *ApJ*, 137, 1005
- Maran, S. P., O’Connell, R. W., Landsman, W. B., Neff, S. G., Roberts, M. S., Smith, A. M.,  
Smith, E. P., & Stecher, T. P. 1993, *BAAS*, 23, 950
- Mathews, W. G., & Baker, J. C. 1971, *ApJ*, 170, 241
- Mathis, J. S., Rumpl, W., & Nordsieck, K. H. 1977, *ApJ*, 217, 425
- McCarthy, P. J., Heckman, T. M., & van Breugel, W. 1987, *AJ*, 93, 264
- McKeith, C. D., Castles, J., Greve, A., & Downes, D. 1993, *A&A*, 272, 98
- McKeith, C. D., Greve, A., Downes, D., & Prada, F. 1995, *A&A*, 293, 703
- McLeod, K. K., Rieke, G. H., Rieke, M. J., & Kelly, D. M. 1993, *ApJ*, 412, 111
- Meurer, G. R., Freeman, K. C., & Dopita, M. A. 1989, *Ap&SS*, 156, 141
- Mihos, J. C., & Hernquist, L. 1994, *ApJ*, 431, L9
- Miyashiro, G. M. 1982, *Zodiac User’s Manual*, 2nd ed.
- Moran, E. C., & Lehnert, M. D. 1997, *ApJ*, 478, 172
- Muxlow, T. W. B., Pedlar, A., Wilkinson, P. N., Axon, D. J., Sanders, E. M., & de Bruyn, A. G.  
1994, *MNRAS*, 266, 455
- Nakai, N., Hayashi, M., Handa, T., Sofue, Y., Hasegawa, T., & Sasaki, M. 1987, *PASJ*, 39, 685
- O’Connell, R. W., Gallagher III, J. S., Hunter, D. A., & Colley, W. N. 1995, *ApJ*, 446, L1
- O’Connell, R. W., & Mangano, J. J. 1978, *ApJ*, 221, 62

- Osterbrock, D. E. 1989, *Astrophysics of Gaseous Nebulae and Active Galactic Nuclei* (University Science Books: Mill Valley, California)
- Osterbrock, D. E., & Martel, A. 1992, *PASP*, 104, 76
- Ostriker, J. P., & Silk, J. 1973, *ApJ*, 184, L113
- Pérez-Olea, D. E., & Colina, L. 1996, *ApJ*, 468, 191
- Pfeffermann, E., Briel, U. G., Hippmann, H., Kettenring, G., Metzner, G., Predehl, P., Reger, G., Stephan, K.-H., Zombeck, M. V., & Chappell, J. 1987, *SPIE Proceedings Vol. 733*, 519
- Phillips, A. C. 1993, *AJ*, 105, 486
- Phillips, M. M., Baldwin, J. A., Atwood, B., & Carswell, R. F. 1983, *ApJ*, 274, 558
- Rice, W., Lonsdale, C. J., Soifer, B. T., Neugebauer, G., Kopan, E. L., Lloyd, L. A., de Jong, T., & Habing, H. J. 1988, *ApJS*, 68, 91
- Rieke, G. H., Lebofsky, M. J., Thompson, R. I., Low, F. J., & Tokunaga, A. T. 1980, *ApJ*, 238, 24
- Rieke, G. H., Loken, K., Rieke, M. J., & Tamblyn, P. 1993, *ApJ*, 412, 99
- Rodriguez, L. F., & Chaisson, E. J. 1980, *ApJ*, 238, 41
- Rohan, M., Morrison, P., & Sadun, A. 1987, in *Star Formation in Galaxies*, ed. C. J. Lonsdale, NASA Conf. Pub. 2466, p. 485
- Scarrott, S. M., Eaton, N., & Axon, D. J. 1991, *MNRAS*, 252, 12P
- Schaaf, R., Pietsch, W., Biermann, P. L., Kronberg, P. P., & Schmutzler, T. 1989, *ApJ*, 336, 722
- Schmidt, G. D., Angel, J. R. P., & Cromwell, R. H. 1976, *ApJ*, 206, 888
- Seaquist, E. R., Bell, M. B., & Bignell, R. C. 1985, *ApJ*, 294, 546
- Seaquist, E. R., & Odegard, N. 1991, *ApJ*, 369, 320
- Shapiro, P. R., & Benjamin, R. A. 1991, *PASP*, 103, 923
- Shen, J., & Lo, K. Y. 1995, *ApJ*, 445, L99
- Shopbell, P. L. 1995, PhD Thesis, Rice University, Houston, Texas
- Shopbell, P. L. 1997, *Zodiac+ User's Manual*, 1st ed.
- Shu, F. H., Ruden, S. P., Lada, C. J., & Lizano, S. 1991, *ApJ*, 370, L31
- Slavin, J. D., & Cox, D. P. 1993, *ApJ*, 417, 187

- Slavin, J. D., Shull, J. M., & Begelman, M. C. 1993, *ApJ*, 407, 83
- Smith, S. J. 1993, *ApJ*, 411, 570
- Smith, S. J., Kennel, C. F., & Coroniti, F. V. 1993, *ApJ*, 411, 581
- Smith, S. J., Kennel, C. F., & Coroniti, F. V. 1993, *ApJ*, 412, 82
- Sofue, Y., Nakai, N., Handa, T., Golla, G., Reuter, H.-P., & Wielebinski, R. 1990, in *The Interstellar Disk-Halo Connection in Galaxies*, ed. H. Bloemen, IAU Symp. 144 (Kluwer Academic Publishers: Dordrecht), p. 9
- Soifer, B. T., Houck, J. R., & Neugebauer, G. 1987, *ARA&A*, 25, 187
- Sokolowski, J. 1992, PhD Thesis, Rice University, Houston, Texas
- Solinger, A. B. 1969, *ApJ*, 155, 403
- Solinger, A. B., & Markert, T. 1975, *ApJ*, 197, 309
- Solinger, A. B., Morrison, P., & Markert, T. 1977, *ApJ*, 211, 707
- Stark, A. A., & Carlson, E. R. 1984, *ApJ*, 279, 122
- Stecher, T. P., *et al.* 1992, *ApJ*, 395, L1
- Strickland, D. K., Ponman, T. J., & Stevens, I. R. 1996, *A&A*, 320, 378
- Suchkov, A. A., Balsara, D. S., Heckman, T. M., & Leitherer, C. 1994, *ApJ*, 430, 511
- Suchkov, A. A., Berman, V. G., Heckman, T. M., & Balsara, D. S. 1996, *ApJ*, 463, 528
- Sulentic, J. W., & Arp, H. C. 1987, *ApJ*, 319, 693
- Sutherland, R. S., Bicknell, G. V., & Dopita, M. A. 1993, *ApJ*, 414, 510
- Tammann, G. A., & Sandage, A. R. 1968, *ApJ*, 151, 825
- Telesco, C. M., Campins, H., Joy, M., Dietz, K., & Decher, R. 1991, *ApJ*, 369, 135
- Telesco, C. M., & Gezari, D. Y. 1992, *ApJ*, 395, 461
- Tielens, A. G. G. M., McKee, C. F., Seab, C. G., & Hollenbach, D. J. 1994, *ApJ*, 431, 321
- Tomisaka, K., & Bregman, J. N. 1993, *PASJ*, 45, 513
- Tomisaka, K., & Ikeuchi, S. 1988, *ApJ*, 330, 695
- Trümper, J. 1984, *Phys. Scripta*, T7, 209

- Tsuru, T., Ohashi, T., Makishima, K., Mihara, T., & Kondo, H. 1990, PASJ, 42, L75
- Tsuru, T., Hayashi, I., Awaki, H., Koyama, K., Fukazawa, Y., Ishisaki, Y., Iwasawa, K., Ohashi, T., Petre, R., Rasmussen, A., & Nousek, J. 1994, in *New Horizon of X-ray Astronomy - First Results from ASCA*, eds. F. Makino and T. Ohashi (Universal Academy Press, Japan), p. 529
- Veilleux, S., Cecil, G., Bland-Hawthorn, J., Tully, R. B., Filippenko, A. V., & Sargent, W. L. W. 1994, ApJ, 433, 48
- Veilleux, S., & Osterbrock, D. E. 1987, ApJS, 63, 295
- Visvanathan, N., & Sandage, A. R. 1972, ApJ, 176, 57
- Visvanathan, N. 1974, ApJ, 192, 319
- Voit, G. M., Donahue, M., & Slavin, J. D. 1994, ApJS, 95, 87
- Waller, W. H., Gurwell, M., & Tamura, M. 1992, AJ, 104, 63
- Watson, M. G., Stanger, V., & Griffiths, R. E. 1984, ApJ, 286, 144
- White III, R. E., & Chevalier, R. A. 1983, ApJ, 275, 69
- Williams, T. B., Caldwell, N., & Schommer, R. A. 1984, ApJ, 281, 579
- Yun, M. S., Ho, P. T. P., & Lo, K. Y. 1994, Nature, 372, 530

Fig. 1.— Flux maps of M82 in the emission lines of (a.)  $\text{H}\alpha$  6563Å and (b.)  $[\text{N II}]$  6583Å, in units of  $\text{ergs cm}^{-2} \text{sec}^{-1}$ , log-scaled between  $-15.5$  and  $-13.0$ . The upper maps represent the total flux in the line at each pixel, while the lower panels represent the flux in the high- (HVC) and low- (LVC) velocity components of the line, in the regions where the line is split (designated by an outline in the upper panel). Splitting of the  $[\text{N II}]$  emission line is only observed south of the disk.

Fig. 2.— Flux map of M82 in the emission line of  $[\text{O III}]$  5007Å, in units of  $\text{ergs cm}^{-2} \text{sec}^{-1}$ , log-scaled between  $-16.0$  and  $-14.2$ . The  $[\text{O III}]$  emission line profiles were fit with single components throughout the field. A contour map of the  $\text{H}\alpha$  flux has been superimposed.

Fig. 3.— Velocity map of M82 in the emission line of  $\text{H}\alpha$  6563Å, in units of  $\text{km s}^{-1}$ . The upper map represents the total velocity of the  $\text{H}\alpha$ -emitting gas at each pixel. In regions of multiple velocity components, the component velocities have been combined with flux weighting to yield an “average” velocity. An ellipse centered on the  $2.2 \mu\text{m}$  nucleus (Waller, Gurwell, & Tamura 1992) has been superimposed on the image. The lower panels represent the velocities in the high- (HVC) and low- (LVC) velocity components of the line, in the regions where the line is split (designated by an outline in the upper panel). Note that the velocity range is much greater for these component panels than for the total velocity map.

Fig. 4.— Flux ratio map of M82 for the ratio of the flux in the emission line of  $[\text{N II}]$  6583Å to the flux in the emission line of  $\text{H}\alpha$  6563Å, log-scaled between  $-0.8$  and  $+0.3$ . A contour map of the  $\text{H}\alpha$  flux has been superimposed.

Fig. 5.— Flux ratio map of M82 for the ratio of the flux in the emission line of  $[\text{O III}]$  5007Å to the flux in the emission line of  $\text{H}\alpha$  6563Å, log-scaled between  $-2.2$  and  $-0.5$ .

Fig. 6.— Rotation curves from the major axis of M82, in order of increasing wavelength. Literature sources include: a.–b. McKeith *et al.* 1993, c. this paper, d.–e. Castles, McKeith, & Greve 1991, f. McKeith *et al.* 1993, g. Beck *et al.* 1978, h. Loiseau *et al.* 1990. A systemic velocity of  $208.7 \text{ km s}^{-1}$  has been subtracted from the Fabry-Perot data.

Fig. 7.— A profile of the peak  $\text{H}\alpha$  emission along a band parallel to and approximately 725 pc south of the major axis of M82, illustrating the bright filaments and underlying diffuse halo component. The dashed line represents a cut through an exponential halo model. Tick marks on the spatial axis are spaced at  $1'$  intervals.

Fig. 8.— A deep  $\text{H}\alpha$  image of M82. Filamentary structure is observed along the minor axis of the galaxy across the entire  $6'$  field. A contour map of the *ROSAT* HRI image has been superimposed; the contours represent 0.5 to 4.0 events per pixel, in thirteen log-spaced increments. The x-ray map has been smoothed with a Gaussian of FWHM  $\sim 12''$ . Tick marks are spaced at  $1'$  intervals.

Fig. 9.— Mosaic of 16 monochromatic frames from the  $\text{H}\alpha$  Fabry-Perot data cube. The field of view is  $3'.5$ . The frames are separated by  $\sim 45 \text{ km s}^{-1}$ , where the frame marked with an asterisk

corresponds roughly to the systemic velocity of the galaxy. The circular region in the southeast corner is a masked ghost from the star in the southwest corner.

Fig. 10.— The radial velocity profile from fits to the  $H\alpha$  line components along the axis of the outflow (position angle of  $150^\circ$ ), from both the Fabry-Perot data and the longslit observations of McKeith *et al.* 1995. A systemic velocity of  $200 \text{ km s}^{-1}$  has been subtracted from all values. The Fabry-Perot points have been interpolated over a band  $7''$  wide through the  $2.2 \mu\text{m}$  nucleus. Dual  $H\alpha$  components are resolved in both the north and south outflow lobes. The shaded region represents a velocity cut along the axis of a two-cone Monte-Carlo simulation.

Fig. 11.— Y-Z cuts along the axes of two Monte-Carlo models of the southern outflow in M82: *a.* a single truncated bubble and *b.* a pair of inclined cones. Dimensions are given in parsecs; arrows denote the direction toward the observer.

Fig. 12.— Comparison of the observed  $H\alpha$  emission and a two-cone Monte-Carlo simulation of the southern outflow in M82. Panel *a* compares the model with the spatial distribution of  $H\alpha$  flux (contour map) and the regions of split  $H\alpha$  lines (grayscale). Panels *b-d* are two-dimensional spectra extracted along the axes drawn in panel *a*, and illustrate the multiple velocity components. The spectrum in panel *b* has been extracted along the axis of the cones, while panels *c* and *d* have been extracted perpendicular to the cone axis, at distances of 650 and 910 pc from the nucleus. Panel *b* is oriented with North at the top; panels *c* and *d* are oriented with West at the top.

Fig. 13.— The  $H\alpha$  flux map from the optical Fabry-Perot data set overlaid with a contour map of the *ROSAT* HRI x-ray image. Tick marks are spaced at  $1'$  intervals. The  $H\alpha$  image is displayed logarithmically between  $10^{-15.5}$  and  $10^{-13.0} \text{ ergs cm}^{-2} \text{ sec}^{-1}$ , while the x-ray contours represent 0 to 5 events per pixel, in 7 equally-spaced increments. The x-ray map has been smoothed with a Gaussian of FWHM  $\sim 2''$ .

Fig. 14.— Reddening-corrected  $[\text{O III}]/H\beta$  versus  $[\text{N II}]/H\alpha$  for a selection of H II regions (circles), H II region models (lines), starburst galaxies (triangles), and AGN (filled polygons). The position of the outflow gas in the southern lobe of the M82 wind is represented by the shaded region. The arrows are oriented in the direction of increasing distance from the nucleus and represent a radial extent of approximately 1 kpc. (Plot adapted from Veilleux & Osterbrock 1987.)

Fig. 15.— Reddening-corrected  $[\text{O III}]/H\beta$  versus  $[\text{N II}]/H\alpha$  grids for a selection of high-velocity shock models. Observations of Seyfert galaxies are shown as open circles; LINERs are shown as filled circles. The grid labeled 'Shock Only' includes only the emission from the shock, while the grid labeled 'Shock + Precursor' includes the contribution of preshock ionization. Emission characteristics of shocks with velocities of  $150\text{--}500 \text{ km s}^{-1}$  are computed. The position of the outflow gas in the southern lobe of the M82 wind is represented by the shaded region. The arrows are oriented in the direction of increasing distance from the nucleus and represents a radial extent of approximately 1 kpc. (Plot adapted from Dopita & Sutherland 1995.)

Fig. 16.— A deep  $H\alpha$  image overlaid with a contour map of the  $2490\text{\AA}$  ultraviolet emission observed by the *UIT*. Tick marks are spaced at  $1'$  intervals.

Table 1. Useful observational values for the galaxy M82. All values are taken from de Vaucouleurs *et al.* 1991, except where otherwise noted.

|                       |   |
|-----------------------|---|
| Designations          | M82, NGC 3034, UGC 5322, ARP 337, 3C 231  |
| Position (2000.0)     | $\alpha = 09^{\text{h}} 55^{\text{m}} 54^{\text{s}}.0$ ; $\delta = 69^{\circ} 40' 57''$ |
| Galaxy type           | I0, Irr II  |
| Dimensions            | $11'.2 \times 4'.3$ ( $10.6 \times 4.1$ kpc)  |
| Position angle        | $65^{\circ}$  |
| Disk inclination      | $81^{\circ}.5$ <sup>a</sup>   |
| Radial velocity       | $203 \pm 4$ km s <sup>-1</sup>  |
| Distance              | $3.63 \pm 0.34$ Mpc <sup>b</sup>  |
| Mass                  | $2.7 \times 10^{10} M_{\odot}$ <sup>a</sup>   |
| Total magnitude       | $B = 9.30 \pm 0.09$   |
| Galactic extinction   | $A_B = 0.13$  |
| Total colors          | $B - V = 0.89 \pm 0.01$<br>$U - B = 0.31 \pm 0.03$                                      |
| Radio luminosity      | $L_{\text{radio}} = 10^{39}$ ergs s <sup>-1</sup> <sup>c</sup>                          |
| Infrared luminosity   | $L_{\text{IR}} = 10^{44}$ ergs s <sup>-1</sup> <sup>c</sup>                             |
| H $\alpha$ luminosity | $L_{\text{H}\alpha} = 2 \times 10^{41}$ ergs s <sup>-1</sup> <sup>d</sup>               |
| X-ray luminosity      | $L_{\text{X-ray}} = 2 \times 10^{40}$ ergs s <sup>-1</sup> <sup>c</sup>                 |

<sup>a</sup>Lynds & Sandage 1963

<sup>b</sup>Freedman *et al.* 1994. For comparison purposes, we will use the standard value in the literature of  $3.25 \pm 0.20$  Mpc (Tammann & Sandage 1968) in this paper.

<sup>c</sup>Watson, Stanger, & Griffiths 1984

<sup>d</sup>Heckman, Armus, & Miley 1990



Table 2. Theoretical and observational characteristics of the Fabry-Perot instruments.

| Constant              |                           | H $\alpha$ + [N II] Observations |                       | [O III] Observations      |                         |
|-----------------------|---------------------------|----------------------------------|-----------------------|---------------------------|-------------------------|
|                       |                           | theoretical                      | experimental          | theoretical               | experimental            |
| Telescope/Instrument: |                           | CFHT + HIFI                      |                       | UH88 + HIFI               |                         |
| $D_{tel}$             | telescope diameter        | 3.6 m                            | ...                   | 2.24 m                    | ...                     |
| $f_{cam}$             | camera focal length       | 90 mm                            | ...                   | 50 mm                     | ...                     |
| Detector:             |                           | IfA CCD + VISACOM <sup>a</sup>   |                       | CCD                       |                         |
| $p_{\mu}$             | pixel size                | 30 $\mu\text{m}$                 | ...                   | 24 $\mu\text{m}$          | ...                     |
| $p''$                 | plate scale               | 0''.86 pix <sup>-1</sup>         | ...                   | 0''.846 pix <sup>-1</sup> | ...                     |
| $n_p$                 | CCD size                  | 256 $\times$ 256 pix             | ...                   | 432 $\times$ 432 pix      | ...                     |
| $t$                   | exposure time             | 450 sec                          | ...                   | 480 sec                   | ...                     |
| Etalon:               |                           | CFHT3                            |                       | SV1                       |                         |
| $\Delta\lambda$       | free spectral range (FSR) | 85 Å                             | 87.9 Å                | 61 Å                      | 55 Å                    |
| $N_R$                 | reflective finesse        | 60                               | 45-50                 | 60                        | ...                     |
| $n$                   | order of interference     | 75                               | 72                    | 91                        | 91                      |
| $\Lambda_v$           | velocity resolution       | 65 km s <sup>-1</sup>            | ...                   | 60 km s <sup>-1</sup>     | ...                     |
| Observations          |                           |                                  |                       |                           |                         |
| $\delta\lambda$       | sampling increment        | 0.96 Å                           | 0.99 Å                | ...                       | 0.67 Å                  |
| $\delta v$            | sampling increment        | 44 km s <sup>-1</sup>            | 45 km s <sup>-1</sup> | ...                       | 40.5 km s <sup>-1</sup> |

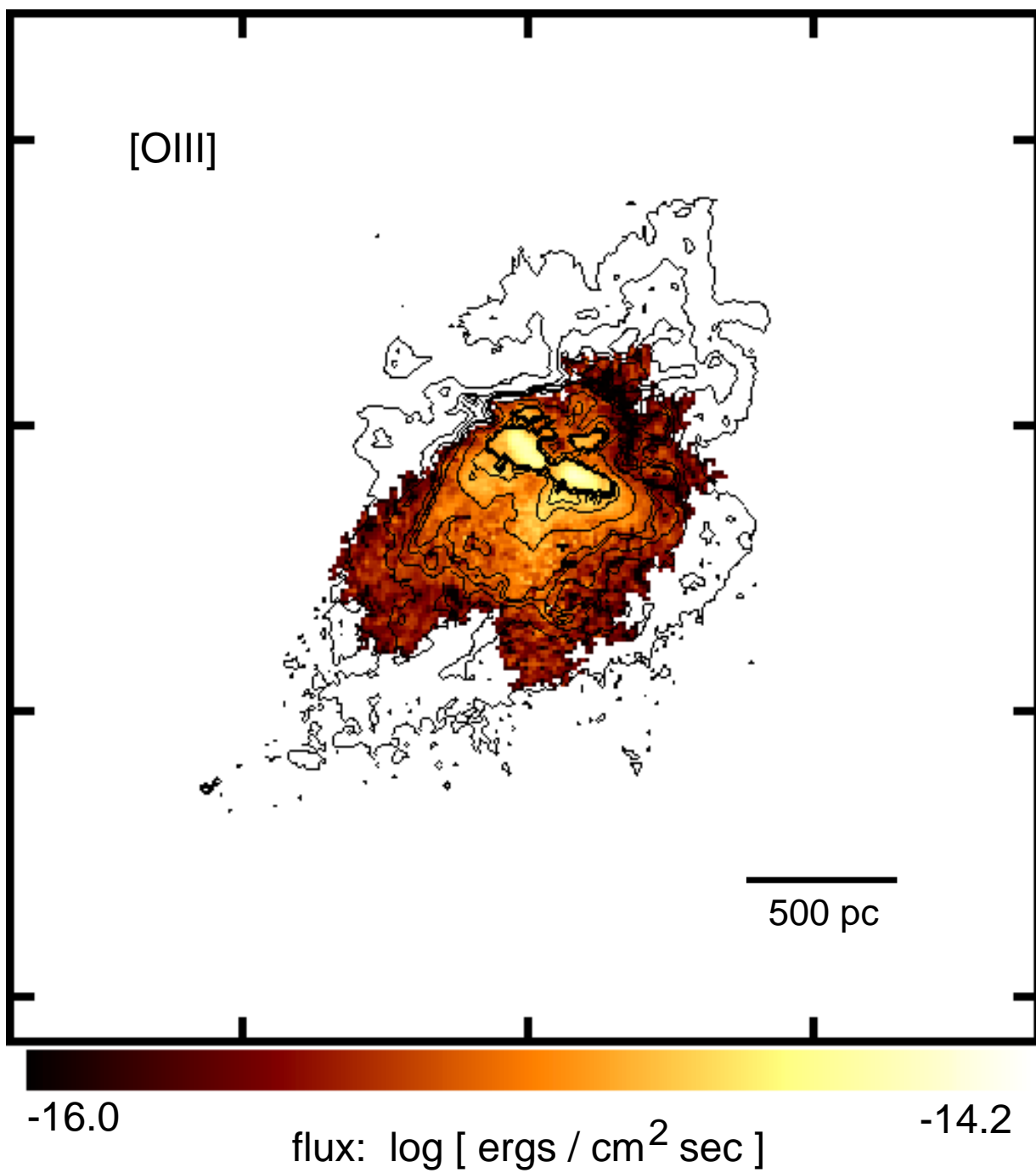
<sup>a</sup>Values include 2 $\times$ 2 binning.

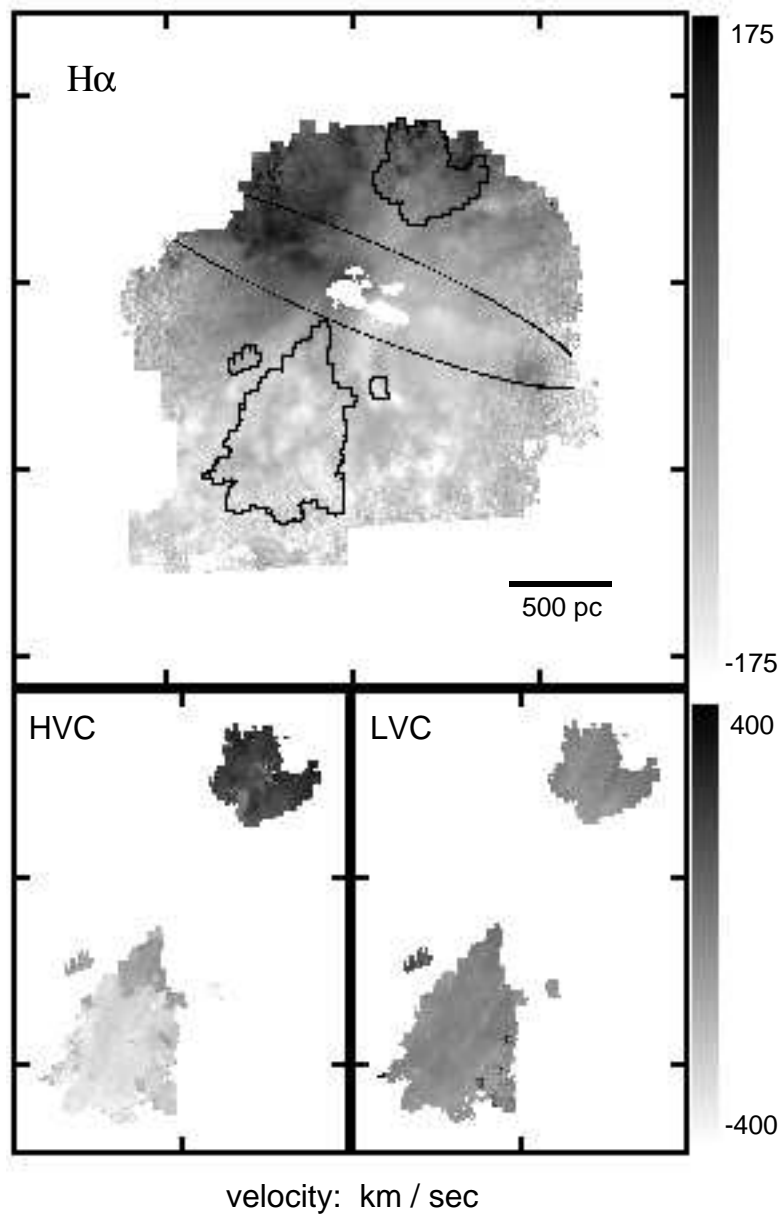
Table 3. Parameters of the two-cone Monte-Carlo simulation which best reproduces the observed kinematics of the southern outflow in M82.

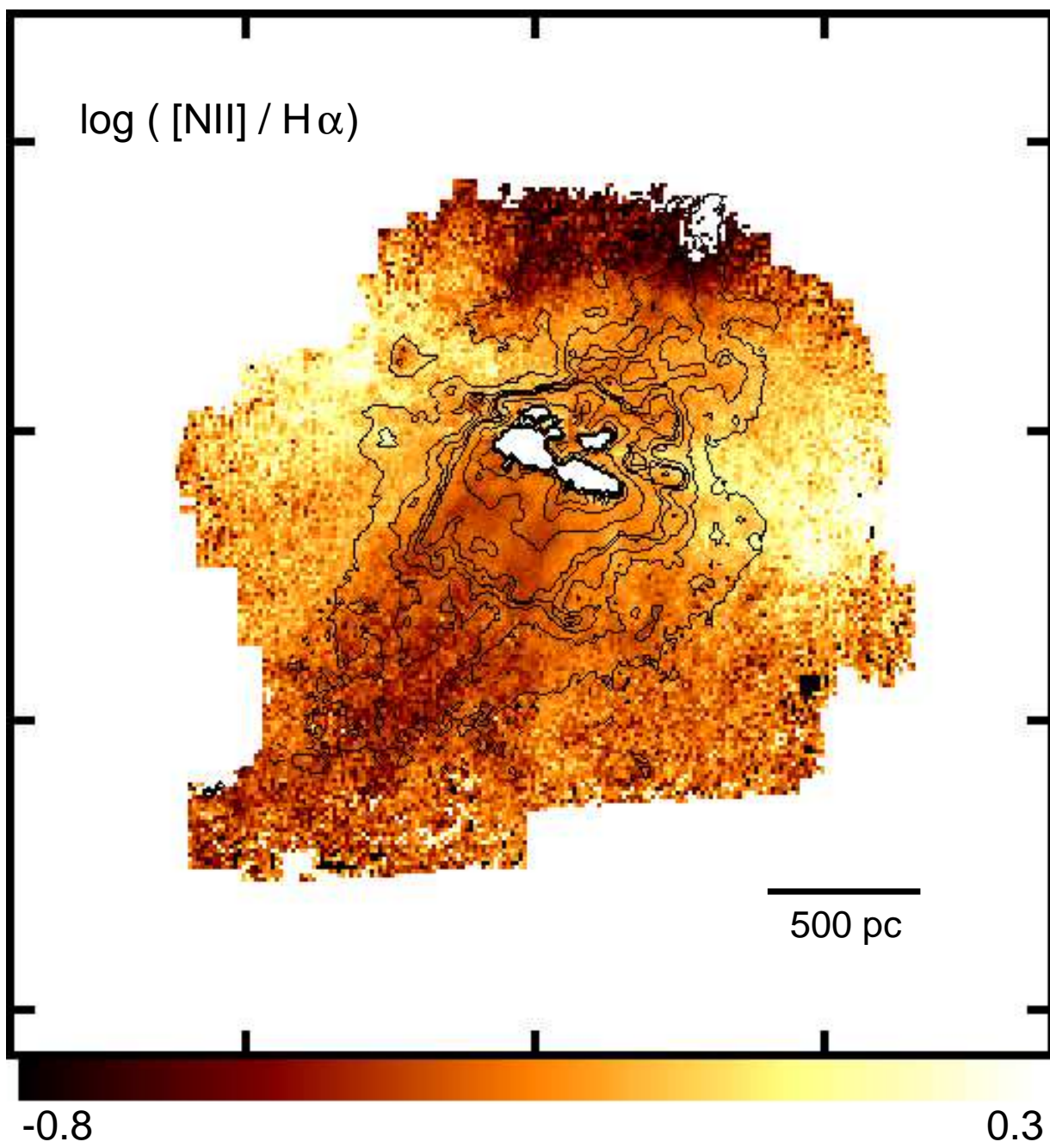
|                   |                               | Inner cone                    | Outer cone  |
|-------------------|-------------------------------|-------------------------------|-------------|
| inner height      | $z_1$ [pc]                    | 0                             | 350         |
| outer height      | $z_2$ [pc]                    | 350                           | 800         |
| minimum diameter  | $D_1$ [pc]                    | 375                           | 390         |
| maximum diameter  | $D_2$ [pc]                    | 400                           | 590         |
| opening angle     | $\alpha$                      | $5^\circ$                     | $25^\circ$  |
| inclination angle | $\iota$                       | $5^\circ$                     | $15^\circ$  |
| position angle    | $pa$                          | $150^\circ\text{--}165^\circ$ | $165^\circ$ |
| radial velocity   | $v(r)$ [km s $^{-1}$ ] ([pc]) | $525 + 0.13r$                 |             |

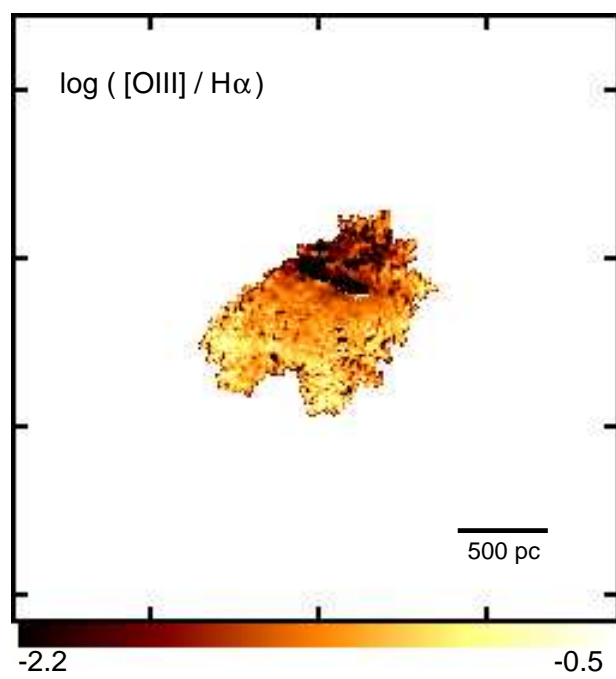
This figure "fig01.jpg" is available in "jpg" format from:

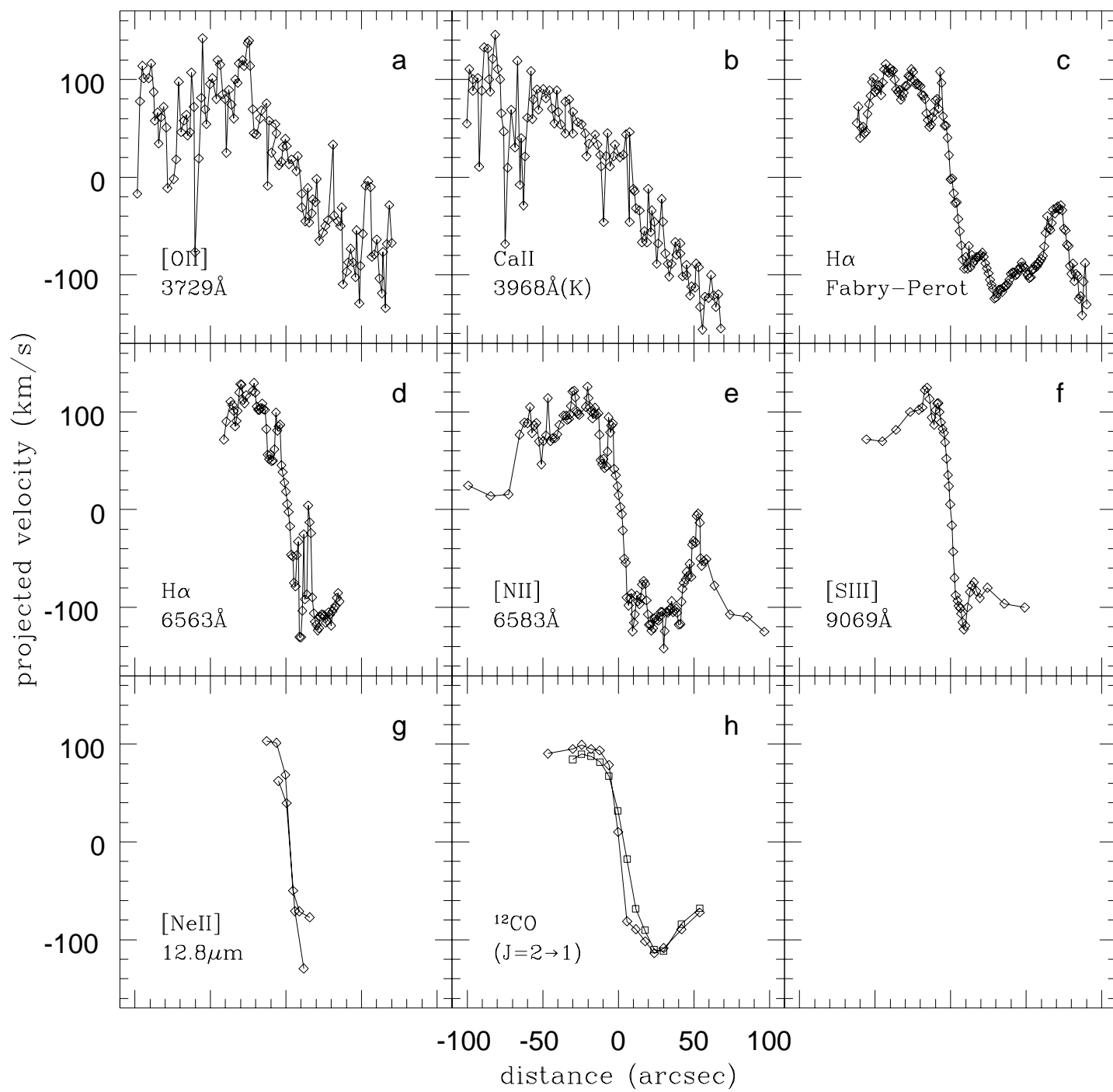
<http://arXiv.org/ps/astro-ph/9708038v2>



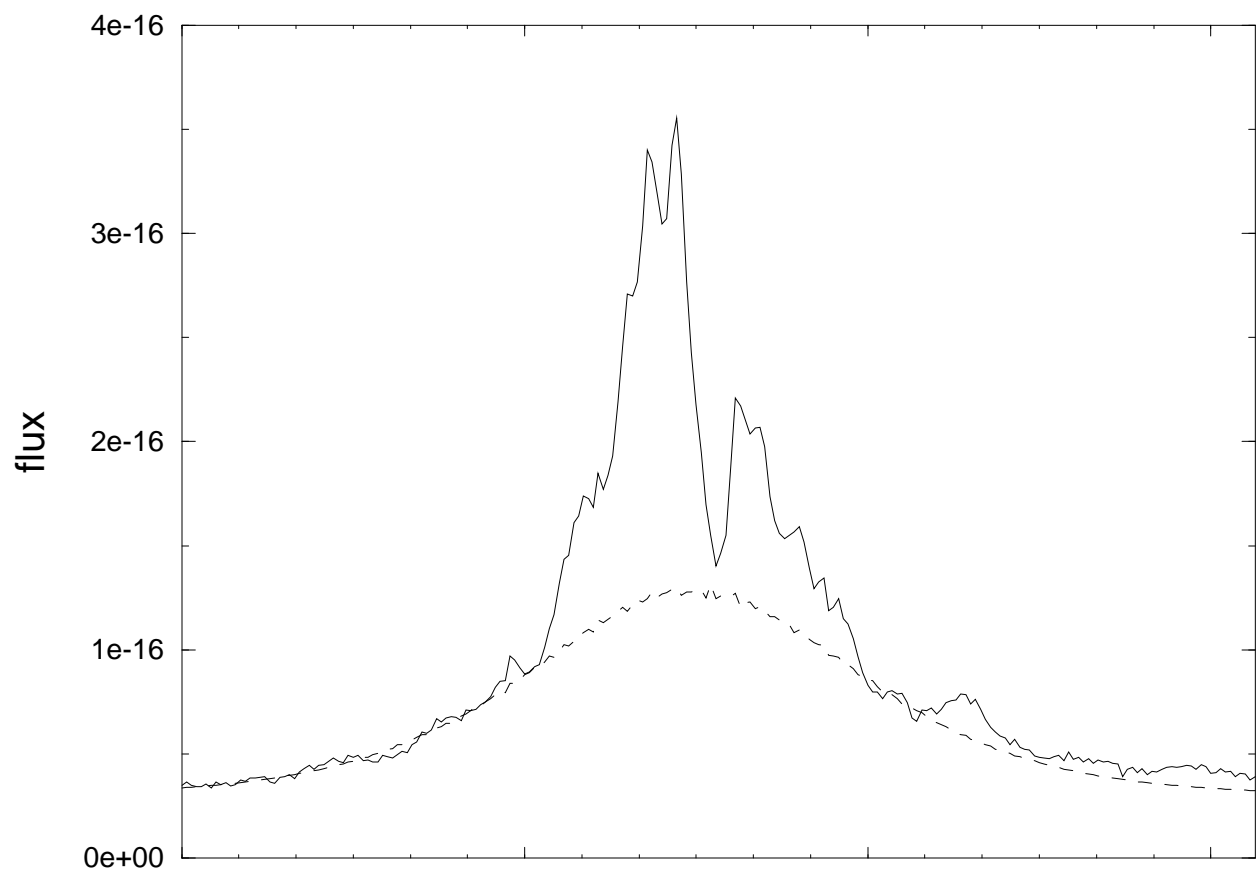










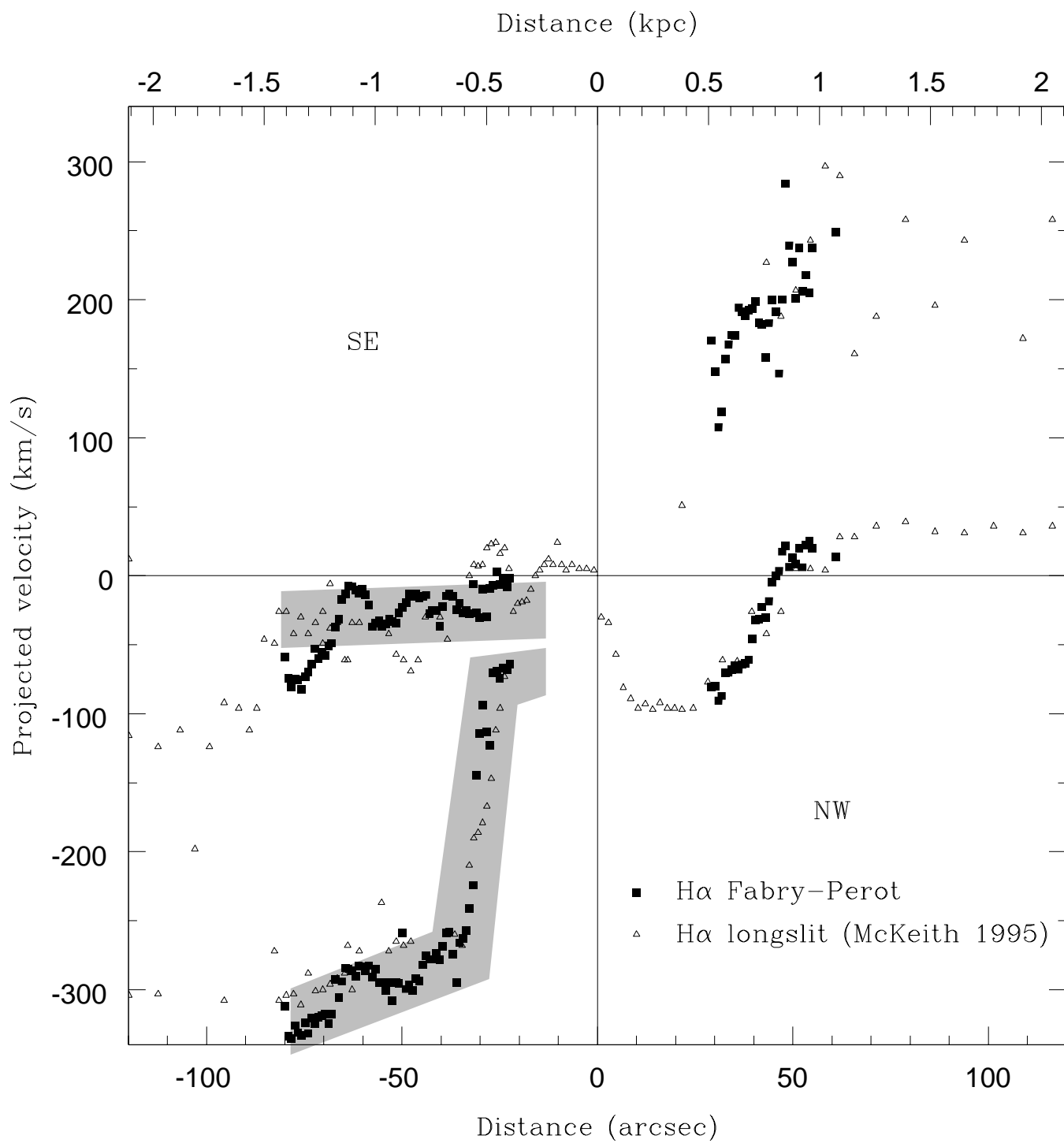


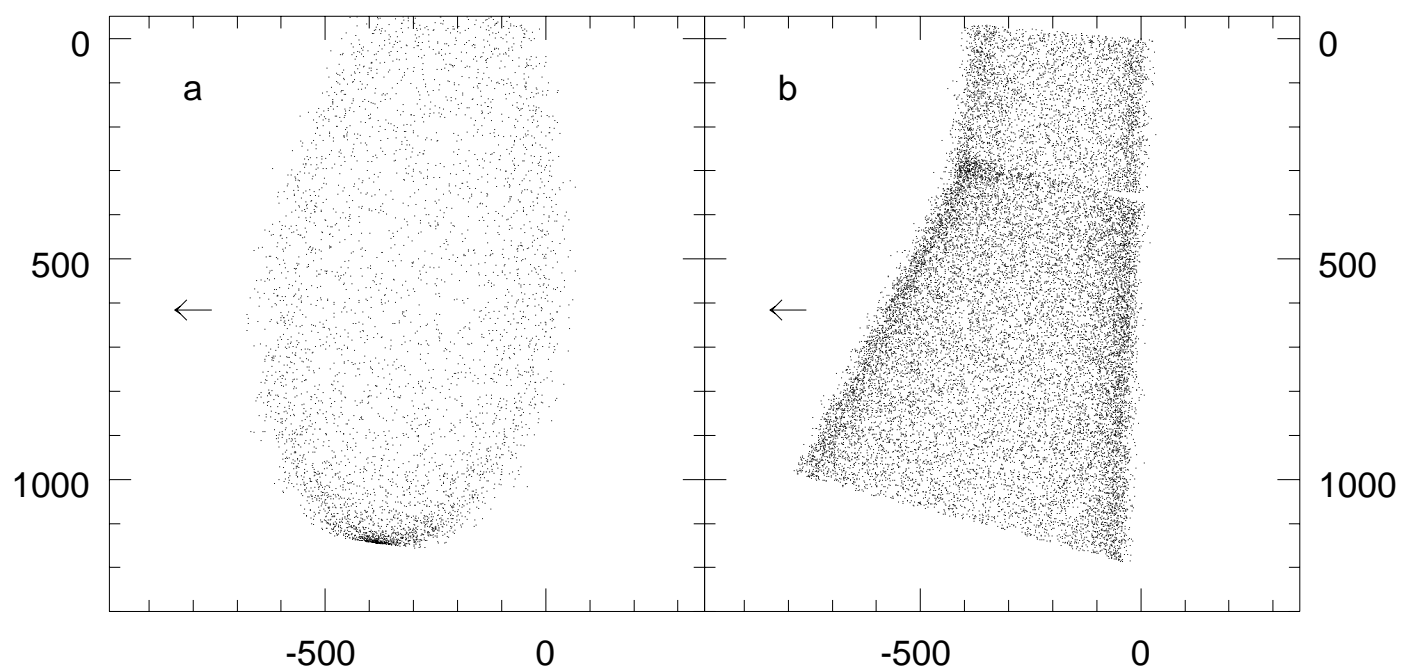
This figure "fig08.jpg" is available in "jpg" format from:

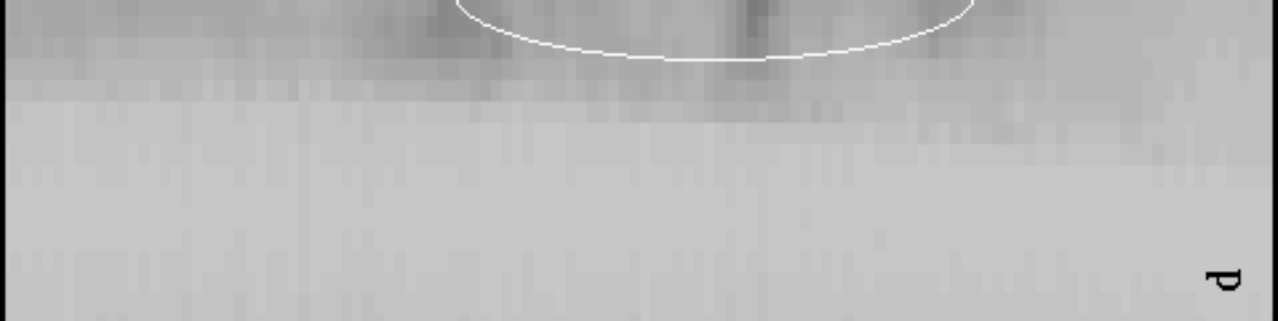
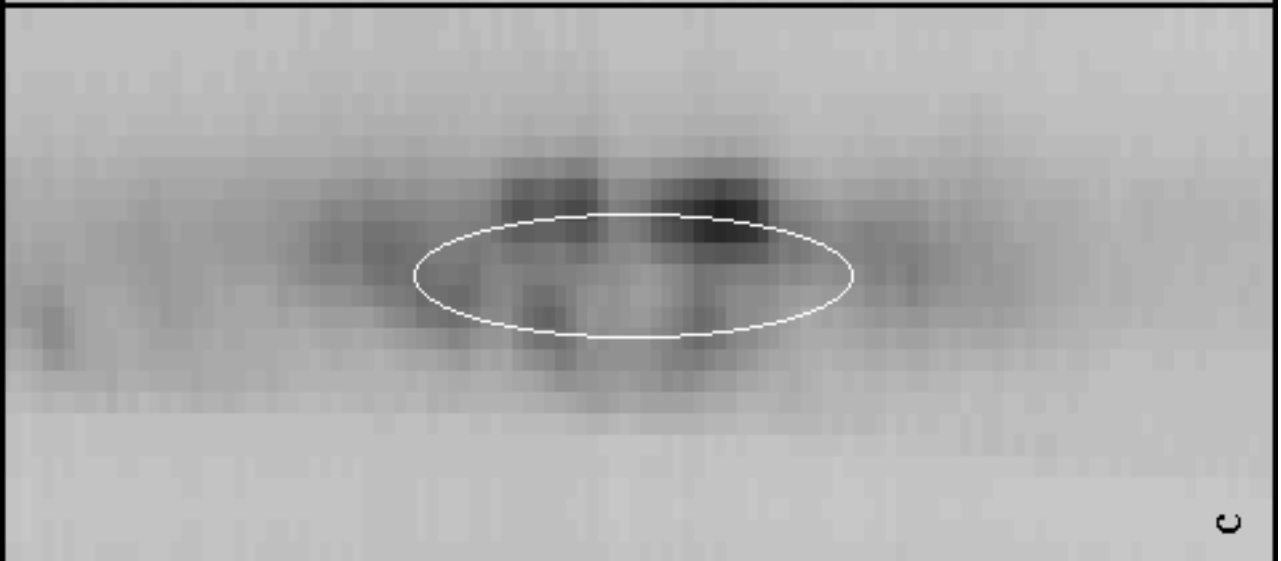
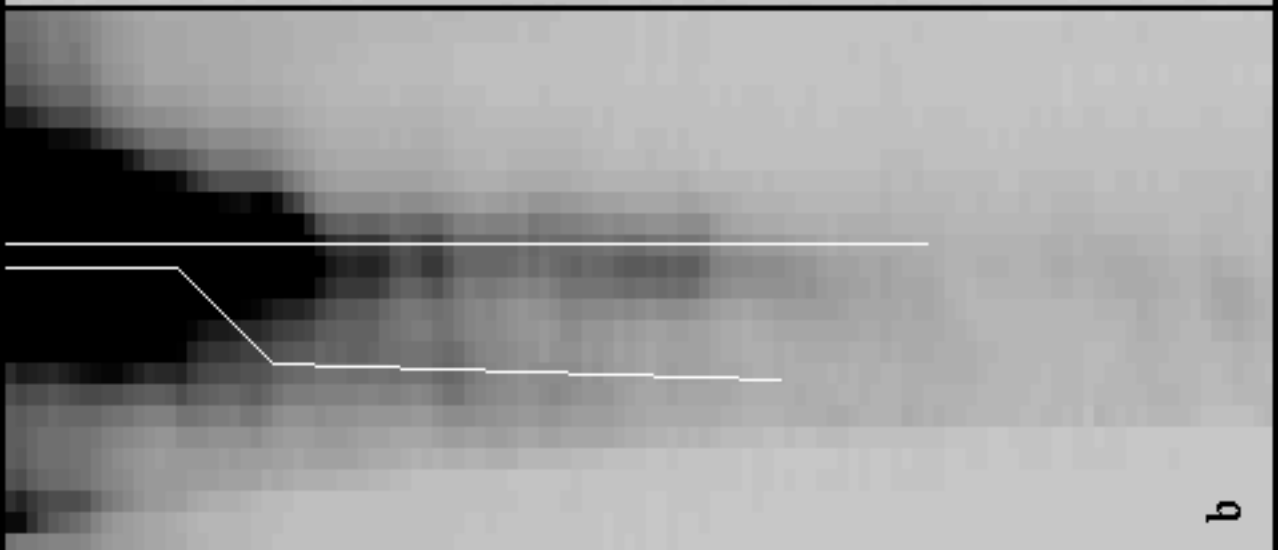
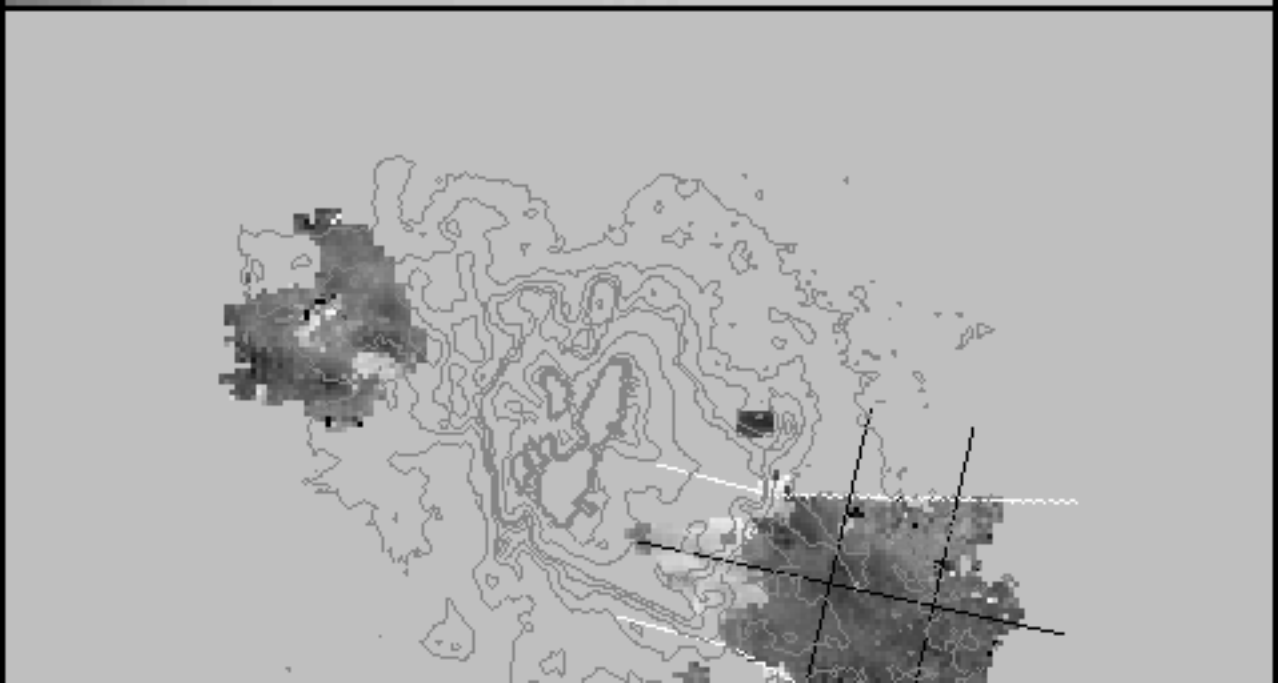
<http://arXiv.org/ps/astro-ph/9708038v2>

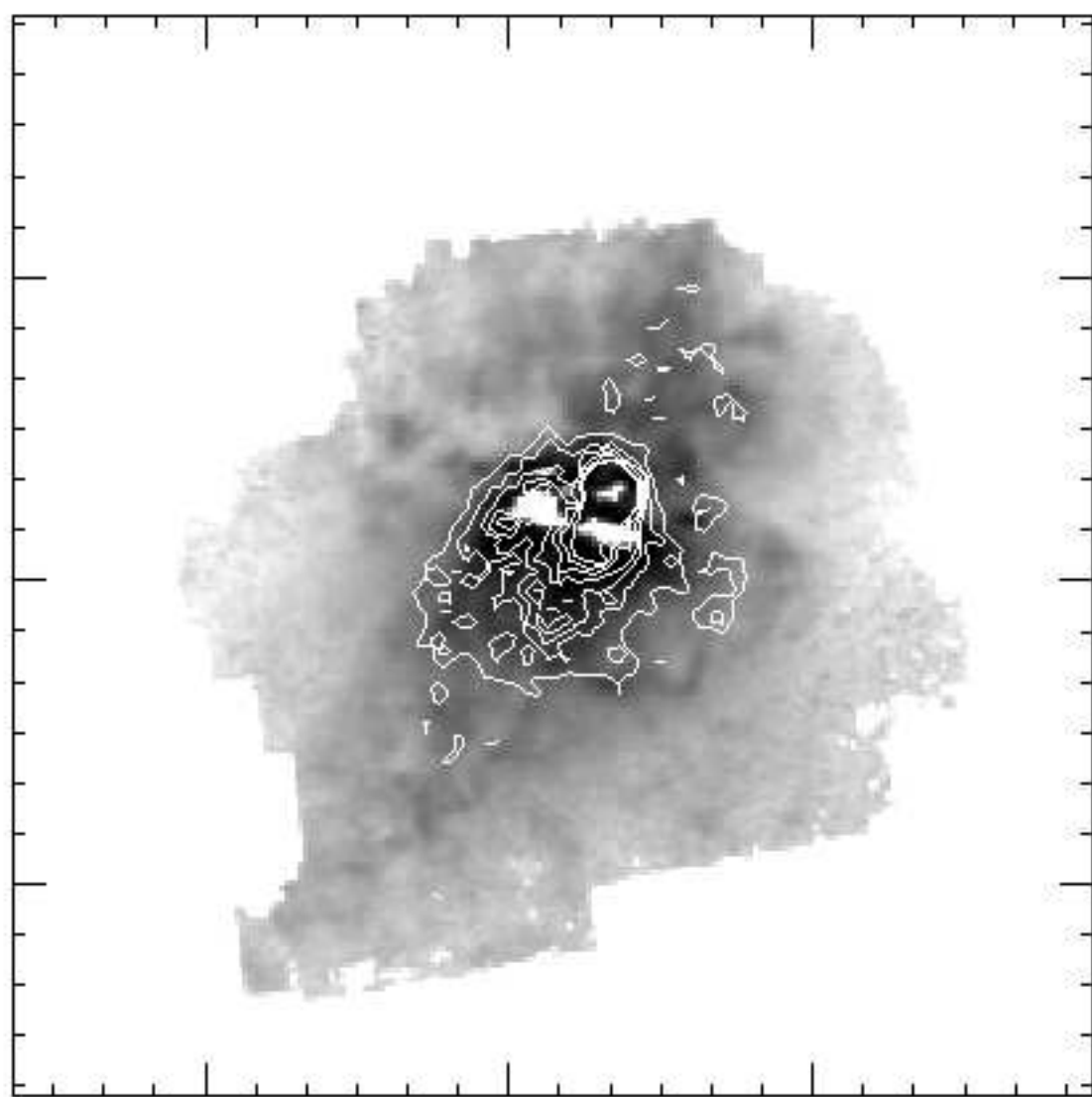
This figure "fig09.jpg" is available in "jpg" format from:

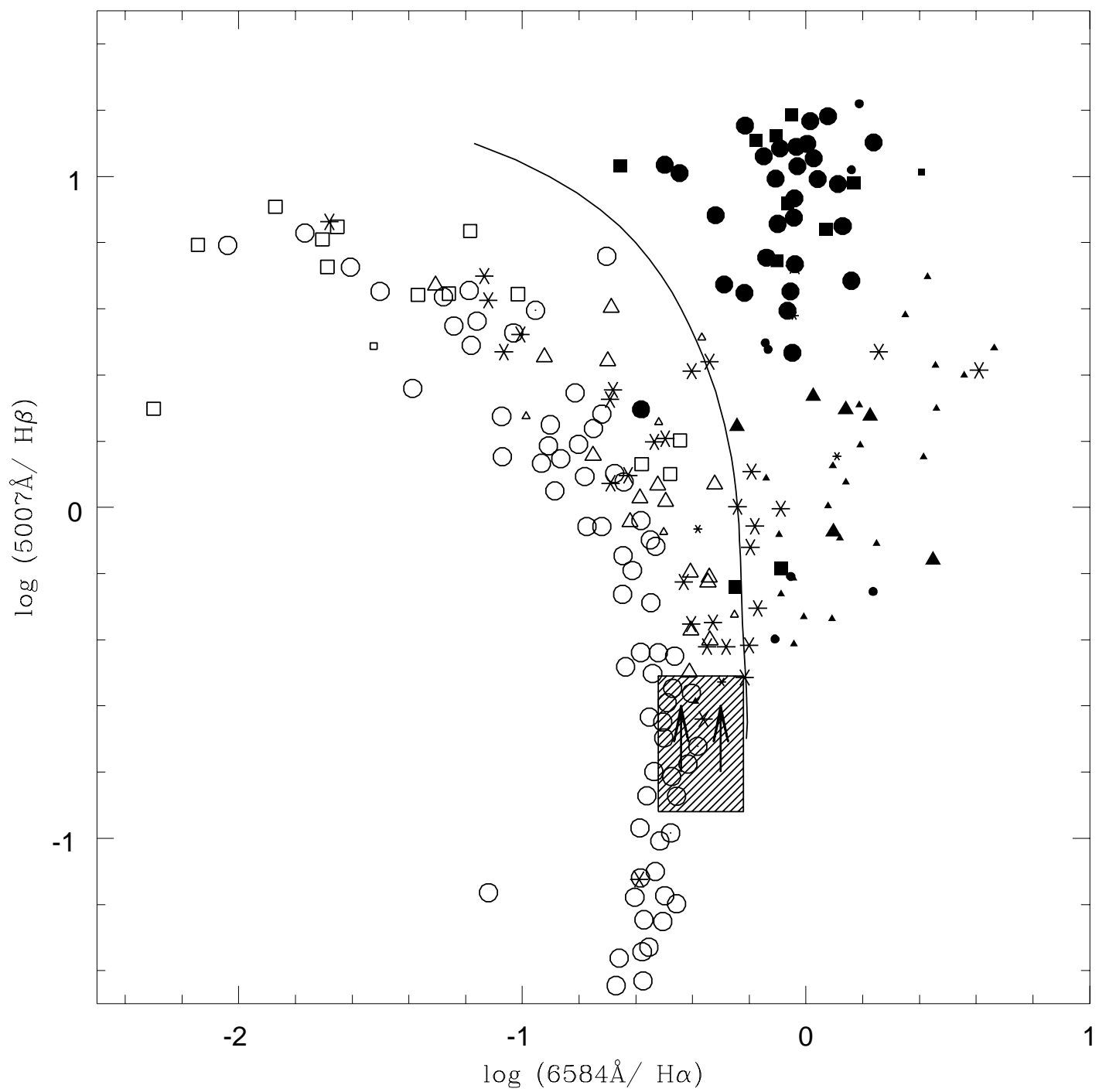
<http://arXiv.org/ps/astro-ph/9708038v2>



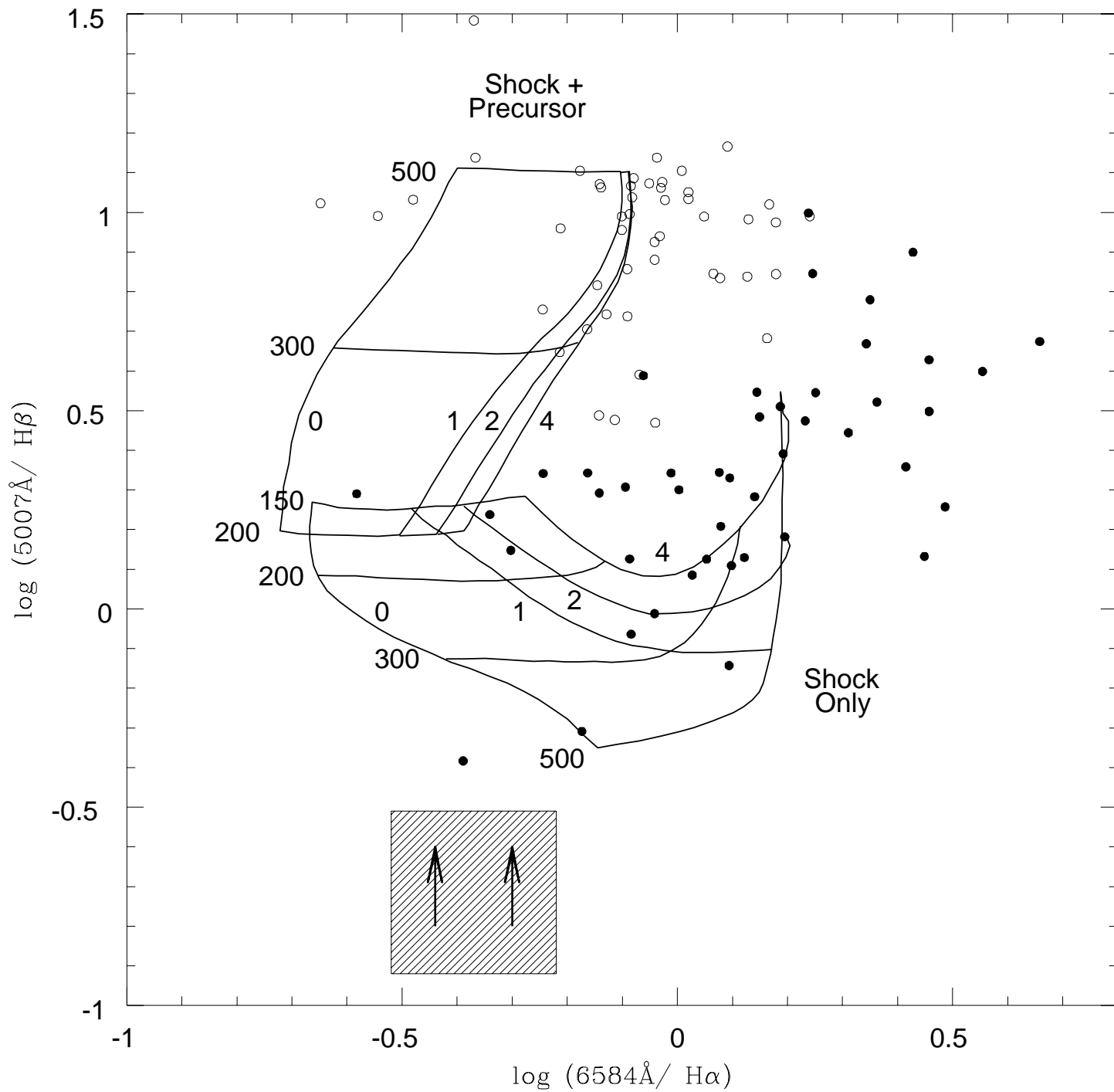












This figure "fig16.jpg" is available in "jpg" format from:

<http://arXiv.org/ps/astro-ph/9708038v2>